



**UNIVERSITÀ DEGLI STUDI DI MILANO
SCUOLA DI SPECIALIZZAZIONE IN FISICA MEDICA
FACOLTÀ DI MEDICINA E CHIRURGIA**

**Diagnostic performance and organ dose evaluation in
radiological diagnosis and follow-up of Ollier
enchondromatosis pediatric patients:
a phantom study**

Relatore:

Prof.ssa Cristina Lenardi

Correlatori:

Dr.ssa Antonella DEL VECCHIO

Prof. Luca Maria SCONFIENZA

Controrelatori:

Dr. Mauro CAMPOLEONI

Dr.ssa Sabina STROCCHI

Tesi di Specializzazione di

Anna PIAI

Matr. S62568

Anno accademico 2019/2020

Contents

CONTENTS	3
ABSTRACT	5
CHAPTER 1 INTRODUCTION	11
1.1. BACKGROUND AND PURPOSE	11
1.2. OLLIER DISEASE	14
CHAPTER 2 MATERIALS AND METHODS.....	15
2.1. EOS IMAGING SYSTEM	15
2.2. PHANTOM DESCRIPTION	17
2.3. EVALUATION OF DIAGNOSTIC PERFORMANCE	19
2.3.a. <i>Simulation of enchondromas</i>	20
2.3.b. <i>Phantom preparation</i>	21
2.3.c. <i>Image acquisitions</i>	21
EOS imaging.....	21
Digital Radiography.....	22
Computed Tomography.....	24
2.3.d. <i>Image quality analysis</i>	25
2.4. REVISION OF DR ACQUISITION PROTOCOL	26
2.5. EVALUATION OF DOSIMETRIC PERFORMANCE.....	28
2.5.a. <i>Dosimetric simulations</i>	28
PCXMC 2.0.....	28
Virtual Dose.....	31
Simulation of EOS acquisitions	33
Simulation of digital radiography acquisitions	34
Simulation of computed tomography acquisitions	36
2.5.b. <i>Dosimetric measurements</i>	36
Characterization and calibration of dosimeters	37
Phantom acquisition	39
Organ dose calculation	41
2.5.c. <i>Effective dose and risk computation</i>	42

CHAPTER 3	RESULTS	44
3.1.	PRELIMINARY STUDY: SIMULATION OF ENCHONDROMAS	44
3.2.	IMAGE QUALITY EVALUATION	45
3.2.a.	<i>Non-expert observers analysis</i>	45
	Analysis of CT images	45
	Analysis of EOS images	46
	Analysis of conventional radiography projections	47
3.2.b.	<i>Analysis of expert observers</i>	48
3.3.	ANALYSIS OF THE DR ACQUISITION PROTOCOL OPTIMIZED FOR FOLLOW-UP	51
3.4.	ASSESSMENT OF DOSIMETRIC PERFORMANCE	53
3.4.a.	<i>Monte Carlo simulations</i>	53
	Simulation of EOS acquisitions	53
	Comparison of DR acquisition protocols	56
	Simulation of CT examination	57
3.4.b.	<i>Dosimetric measurements with TLDs</i>	58
	Preliminary TLD characterization	58
	Calibration of TLD dosimeters	59
	Organ dose measurements and comparison with simulations	64
3.4.c.	<i>Comparison of imaging techniques</i>	69
3.4.d.	<i>Effective dose and risk assessments</i>	71
CHAPTER 4	DISCUSSION AND CONCLUSIONS	74
	Diagnostic performance	74
	Optimization of digital radiography acquisition protocol	76
	Dosimetric performance	77
	Effective dose and risk assessment	81
	Limitations of the work	83
	Conclusions	84
	INDEX OF FIGURES, TABLES AND GRAPHS	86
	THE FIGURES	86
	THE TABLES	89
CHAPTER 5	BIBLIOGRAPHY	91

Acronyms

ALARA	As Low As Reasonably Achievable
AP	Antero-Posterior
CT	Computed Tomography
CV	Coefficient of Variation
DAP	Dose-Area Product
DDREF	Dose and Dose Rate Effectiveness Factor
DR	Digital Radiography
DRL	Diagnostic Reference Level
<i>E</i>	Effective dose
EI	Exposure Index
FSD	Focus-to-Skin Distance
HU	Hounsfield Unit
HVL	Half-Value Layer
ICRP	International Commission on Radiological Protection
IR	Interventional Radiology
LAR	Life Attributable Risk
LL	Lateral
LLE	Loss of Life Expectancy
MC	Monte Carlo
OSL	Optically Stimulated Luminescence Dosimeters
PA	Postero-Anterior
PACS	Picture-Archiving and Communication System
PMMA	PolyMethyl MethAcrylate
RDIM	Radiation Dose Index Monitoring
RDSR	Radiation Dose Structured Report
REID	Risk of Exposure-Induced Death

ROI	Region Of Interest
SD	Standard Deviation
SdNR	Signal-difference-to-Noise-Ratio
TLD	ThermoLuminescent Dosimeter

Abstract

The European Council Directive 2013/59/Euratom included pediatric exposure in the special practices for which appropriate medical radiological equipment and practical techniques have to be ensured. Children are generally more sensitive to X-rays than adults, mainly due to rapid cell growth and replication, and a longer lifespan after exposure. Hence, the optimization of protection is a priority factor and it shall involve all the practical aspects of medical radiological procedures, from the selection of equipment to quality assurance and the assessment of patient doses. These concepts are strongly endorsed by health care organizations dedicated to providing safe and high-quality pediatric imaging, particularly in modalities involving higher radiation doses, such as computed tomography and fluoroscopy.

IRCCS Istituto Ortopedico Galeazzi is a reference center for the diagnosis and treatment of pediatric orthopedic and traumatological diseases, including orthopedic tumors. Ollier disease is a rare skeletal disorder characterized by the presence of multiple enchondromas, which are intraosseous, usually benign, cartilage tumors. Although the enchondromas start out as benign, they may become malignant, so children affected by the disease undergo multiple radiographs over time. Special effort is thus required to reduce the risk of radiation-induced cancers, and the benefit provided by radiological procedures has to be properly balanced with the health risk associated with ionizing radiation. The principal aim of this study was to evaluate the applicability of a relatively novel low-dose technique based on a slot scanning technology (EOS imaging system), for the diagnosis and follow-up of Ollier disease. For this purpose, a 5-year-old anthropomorphic phantom was specifically purchased to evaluate the diagnostic and dosimetric

performances of the system. Digital radiography (DR) and computed tomography (CT), the current gold standards for diagnosis and monitoring, were evaluated for comparison.

Ollier enchondromas were simulated with homemade bone structures stuck on the phantom, which was then imaged with DR, CT, and the EOS system at three different scanning speeds. To assess the diagnostic power of the imaging system, non-expert observers and experienced radiologists measured the inserts dimensions and compared them with those derived from CT and DR. Interobserver and intermodality reproducibilities were evaluated through Bland-Altman analysis. Furthermore, the accuracy in the size estimation was investigated by comparing the measured dimensions with the real ones. Dosimetric evaluations were performed for each imaging technique through Monte Carlo (MC) simulations and in-phantom measurements with thermoluminescent dosimeters (TLDs). The validation of MC simulations with TL dosimetry was necessary for the EOS system as no reference was found in the literature. Three speed levels of the EOS X-ray tube, and two DR acquisition protocols, respectively suited for diagnosis and follow-up, were investigated. The measured organ doses were used to calculate effective dose according to the ICRP 103 recommendations. Risks of radiation-induced cancers were estimated in the form of Lifetime Attributable Risk (LAR).

The EOS system performed similarly to DR and CT in both detection and measurement of enchondromas-like inserts. Excellent intermodality reliability and interobserver reproducibility were obtained for each imaging technique. EOS fast protocol provided a reduction of effective and organ doses with respect to DR acquisitions performed with the diagnostic protocol. When the DR protocol optimized for follow-up was considered, instead, no

significant dose sparing was observed, neither in organ doses nor in effective dose. CT doses were considerably higher than doses of EOS and DR, regardless of the acquisition protocol or speed level. Comparable LARs were observed for EOS acquisitions performed with the fast protocol and DR examinations with the follow-up protocol. DR diagnosis protocol was found to be equivalent, in terms of radiological risk, to the EOS intermediate speed level. The risk associated with CT examinations was two orders of magnitude higher than of the other techniques.

This work showed that the EOS system has the same diagnostic capability as DR and CT to detect and measure enchondromas-like inserts in a pediatric phantom, but delivering lower doses. Although no dose reduction was found with respect to DR follow-up protocol, EOS fast protocol still provides low doses, and the two techniques were found to be equivalent in terms of LAR. Thus, it may be considered a valid solution for both the diagnosis and follow-up of patients with Ollier disease or other bone pathologies, allowing easier and faster exams, which is a crucial aspect in pediatric applications.

Chapter 1 Introduction

1.1. Background and purpose

Nowadays, radiological imaging is an essential element in medicine, and it plays a critical role in the diagnosis and treatment of many life-threatening diseases as well as in several emergency situations. Outstanding growth in the use of computed tomography and interventional radiology (IR) procedures has taken place over the last 20 years and radiological imaging of children has been shown to be among the fastest growing areas in the last few years. Notwithstanding, the huge benefit provided by radiological procedures has to be balanced with the health risk associated with the use of ionizing radiation. This is of particular importance in children, who are generally more sensitive to X-rays than adults, mainly due to both rapid cell growth and replication, and a longer lifespan after exposure [1].

Radiation protection in medical exposures is based on two general principles, justification and optimization, which have been established by the International Commission of Radiological Protection (ICRP) [2], and adopted by the EC Council Directive 2013/59/EURATOM [3]. These concepts are strongly endorsed by health care organizations dedicated to providing safe and high quality pediatric imaging, particularly in modalities involving higher radiation doses, such as computed tomography and fluoroscopy [4,5].

The justification principle requires that medical exposure shall show a sufficient net benefit, weighing the total potential diagnostic or therapeutic benefits it produces against the individual detriment that it may cause, taking into account the efficacy, benefits and risks of available alternative

techniques having the same objective but involving no or less exposure to ionizing radiation.

Optimization is the most challenging process in radiation protection procedure and it is the aim of keeping the magnitude of individual doses due to medical exposure for radiodiagnostic, interventional radiology, planning, guiding and verification purposes as low as reasonably achievable (ALARA), consistent with obtaining the required medical information, taking into account economic, social and psychological factors.

The diagnostic reference levels (DRLs) are one of the main operational tools for optimization of patient protection in radiological imaging. Council Directive 2013/59/Euratom has strictly required Member States their revision and it has promoted the establishment of national DRL values. In 2018, the European Commission embraced these recommendations with the publication of “Radiation Protection 185: European Guidelines on Diagnostic Reference Levels for Paediatric Imaging” [6], which proposes basic instructions on how to establish and to use DRLs for pediatric X-ray examinations. To implement ALARA principle, ICRP Publication 93 [7] introduced the concept of image quality classes. Not all the medical imaging tasks require indeed the same level of image quality or diagnostic information. For instance, follow-up does not require the same level of image quality as that required for diagnosis. For tasks such as follow-up studies, a slight degradation of image quality can be accepted in favor of dose reduction.

This study is part of the ongoing – and constantly developing – optimization process at IRCCS Ospedale San Raffaele and IRCCS Istituto Ortopedico Galeazzi. Its principal aim is to evaluate the possible application of an X-rays scanning device (EOS), a relatively novel low-dose imaging technique, for the

diagnosis and follow-up of Ollier disease, a rare pediatric skeletal disease. Different works [8–10] have demonstrated EOS to considerably reduce the dose compared to conventional radiography in scoliosis examinations, and this work attempts to extend these results also for the evaluations of bone lesions.

At present, the diagnosis and monitoring of Ollier disorder is mainly based on radiological examinations, with patients undergoing multiple radiographs during childhood. The performance of the EOS system is compared in terms of image quality and dose assessments with those of computed tomography and digital radiography, which are the current gold standards for evaluation of the disease.

Image quality analysis, involving two radiologists, was first considered. Different studies demonstrated the excellent performance of EOS imaging in the evaluation of scoliosis and spine alignment [11–14]. However, the technique is not routinely used for diagnostic X-ray examinations, and no comprehensive studies to determine whether this system can be used for other anatomical regions have been undertaken. Abdi et al. [15] evaluated the potential use of the system for clinical diagnosis of chest and knee examinations, while its diagnostic accuracy in identifying and measuring bone tumors has not been investigated previously.

Then, organ doses were estimated for each imaging technique, both with MC simulations and with experimental in-phantom measurements. During recent years, various researchers have performed studies on the determination of the patient dose due to EOS examinations. However, the majority of these studies only use modeling software [16–19] instead of direct measurements, and mainly focus on effective dose evaluations rather than on investigation of organ doses. Furthermore, in-phantom evaluations of organ doses in

pediatric patients mostly focus on CT [20–23], while only a few studies performed direct measurements of organ doses in conventional radiography and EOS [8,10,24].

An anthropomorphic phantom was used for both image quality evaluation and dosimetric measurements. Since no humans were involved in the study, institutional review board approval was not needed.

1.2. Ollier disease

Ollier disease (World Health Organization terminology), also known as enchondromatosis, is a rare nonhereditary pediatric disorder characterized by the presence of multiple intraosseous, usually benign cartilage tumors, called enchondromas [25]. Enchondromas mostly develop in the metaphysis of long bones in close proximity to growth plate cartilage. Cartilage lesions can be extremely variable, in terms of size, number, location, evolution of enchondromas, age of onset and of diagnosis, requirement for surgery. When enchondromatosis is associated with soft tissue hemangiomas, the condition is known as Maffucci syndrome. The prevalence of Ollier disease is estimated to be 1/100000, while there are about 200 reports of Maffucci syndrome [26]. To give an order of magnitude, in the last decade (2009-2019) an average of 5.14 million live births per year was recorded in the European Union [27], which corresponds to about 50 new cases per year.

Clinical manifestations in Ollier disease often appear in the first decade of life and usually start with the appearance of visible masses embedded within phalanges, metacarpal and metatarsal bones. Clinical problems related to enchondromas depend on the extent of skeletal involvement and include skeletal deformities, often associated with pathological fracture, limb-length

discrepancy, and the potential risk for malignant transformation to chondrosarcoma [28,29].

The diagnosis of Ollier disease is mainly based on clinical and radiological evaluations. Additional investigations, such as scintigraphy, ultrasound or magnetic resonance imaging are not useful for establishing the diagnosis [30]. Radiographs typically show an irregular distribution of multiple, radiolucent, homogeneous lesions with an oval or elongated shape and a well-defined, slightly thickened, bony margin.

One of the crucial points of Ollier disease is that enchondromas may become malignant, so children affected by Ollier disease undergo multiple radiographs over time. Thus, the need for accurate assessment of enchondromas has to balance with the risk associated with repeated radiation exposure, which is a major concern given the high radiosensitivity of children.

Chapter 2 Materials and Methods

The performance of the EOS system is compared with those of CT and DR in terms of both image quality and delivered doses. Since EOS imaging technique is relatively novel and far less common than CT and DR, in Section 2.1. a description is provided. In Section 2.2. the used phantom is introduced. The following Sections are dedicated to image quality measurements and dosimetric assessments.

2.1. EOS imaging system

EOS is a biplane X-ray imaging system manufactured by EOS imaging (formerly Biospace Med, Paris) (Figure 1). It uses a slot-scanning technology, based on Nobel prize-winning work of physicist Georges Charpak on

multiwire proportional chambers, to produce a high-quality image with less radiation than standard imaging techniques [31]. The two X-ray tubes, located at 90°, allow the acquisition of simultaneous AP and LL 2D images of the whole body. The sterEOS software, bundled with the EOS imaging system, makes it possible to perform 3D reconstruction of bone structures [12,32]. The images are taken whilst the patient is in an upright (standing, seated or squatting) position, allowing the spine and lower limbs to be examined under normal weight-bearing conditions. The full length of the body (up to 175 cm) can be imaged with a single fast acquisition, removing the need for digital stitching/manual joining of multiple images. Furthermore, since the X-ray sources move in synchronous fashion, true-to-size images can be acquired, avoiding the magnification error inherent in teleradiography, due to the single-source divergent X-ray beam [31].

The scan has a variable duration of up to twenty seconds, and different scanning speeds are available. Since the radiation dose is directly related to the scan time, the selection of the speed level affects the patient dose.

With the effort to further decrease the radiation dose, a new *Microdose* acquisition protocol has been recently developed [33], which has shown promising results in the evaluation of scoliosis [19,34,35].



Figure 1 EOS imaging system.

2.2. Phantom description

The five-year-old CIRS ATOM phantom was used for both image quality evaluation and dosimetric measurements. CIRS ATOM phantoms are a full line of anthropomorphic, cross sectional dosimetry phantoms designed to investigate organ dose. Six models are available: newborn, 1-year, 5-year and

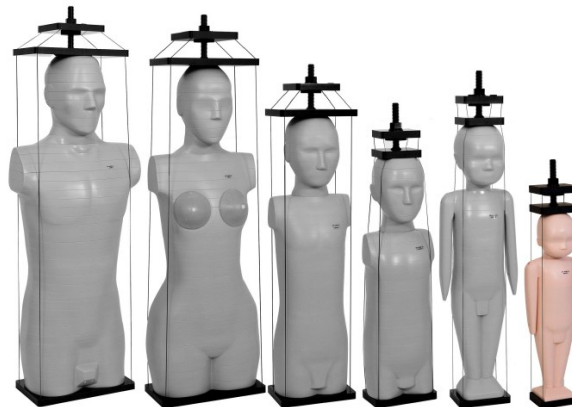


Figure 2 CIRS ATOM dosimetry phantom family. From left to right the adult male, adult women, pediatric 10-year-, 5-year-, 1-year-old and newborn models.

10-year old pediatric phantoms as well as adult male and female phantoms, as shown in Figure 2 [36].

The phantom is sectional in design with 25 mm thick sections. The sectional surfaces are flat and smooth, resulting in minimal air interfaces between the slabs. Tissue-equivalent epoxy resins are used in all aspects of the phantom. The tissues simulated are soft tissue, average bone, cartilage, spinal cord, spinal disks, lung, brain and sinus. Bones are homogeneous and formulated with materials based on the appropriate bone composition typical of the age, since in pediatric patients the red bone marrow is distributed throughout the skeletal system compared with adults.

The 22 radiosensitive internal organs reported in Table 1 are provided with 5 mm diameter holes designed to host detectors for organ dose evaluation.

Organ	Number of detector holes	Organ	Number of detector holes
Eyes	2	Pancreas	3
Brain	10	Kidneys	10
Thyroid	4	Adrenals	3
Heart	2	Intestine	8
Thymus	3	Ovaries	2
Lungs	28	Uterus	2
Liver	18	Urinary Bladder	6
Gallbladder	2	Testes	2
Spleen	4	Prostate	1
Esophagus	3	Breasts	2
Stomach	10	Active Bone Marrow	65

Table 1 Internal organs provided with holes for detector placement and number of allowed dosimeters for the 5-year-old dosimetry phantom model.

TLDs, MOSFETs, Landauer Optically Stimulated Luminescence Dosimeters (OSLs), ion chambers, diodes as well as films, are supported by the phantom. The positions of the holes are set on anatomical information about the average position of the 22 organs, and are optimized for precise calculation using the minimum number of detectors necessary. Each hole is provided with a unique hole ID number, shown on the relative section, as shown in Figure 3. Holes are filled with 5 mm diameter x 25 mm long solid plugs of corresponding tissue (soft tissue, bone, lung, and brain).

TLDs type GR-200A were used in this study. To ensure a minimum air interface between the dosimeters and tissue, some solid plugs were specifically cut so the TLD could be sandwiched between the cut plug and the subsequent phantom section. This was crucial to ensure reliable dosimetric measurements, since the presence of air could skew the results.

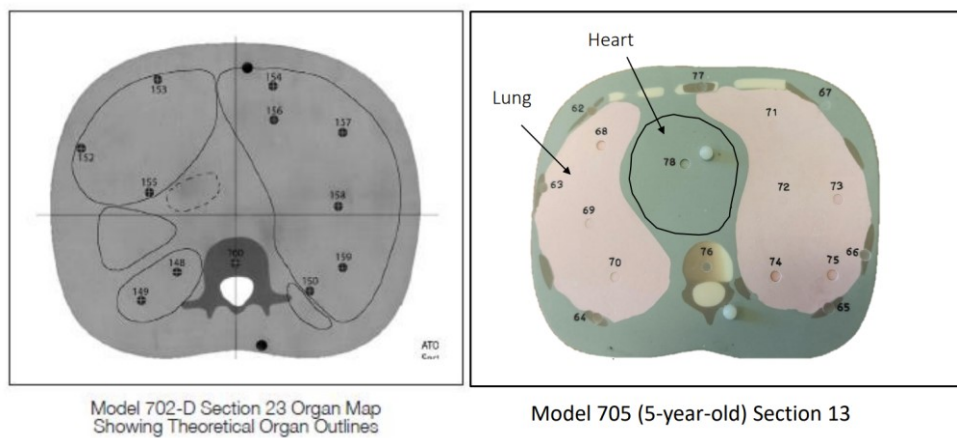


Figure 3 Example of holes position and organ identification in CIRS ATOM dosimetry phantoms. The selection of positions is supported by anatomical information and each hole is provided with a unique ID number.

2.3. Evaluation of diagnostic performance

A phantom study was designed to assess EOS performance in detecting Ollier enchondromas. DR and CT were considered for comparison. The following

Sections describe the steps of the study from the simulation of enchondromas to image quality analysis.

2.3.a. Simulation of enchondromas

Ollier enchondromas were simulated with minced pieces of chicken bone and cartilage, packed in conventional kitchen plastic foil to create ovoidal masses. Chicken bone was chosen in order to reproduce the attenuation of the cartilage lesions. To verify the suitability of this solution, attenuations (as Hounsfield Units (HUs)) of the simulated enchondromas, of the phantom's bone, of pediatric cartilage, and of pediatric bone were measured from CT scans and compared.

Cartilage HUs were measured from whole-body CT scans of five children, by placing regions of interest (ROIs) in the fibrocartilaginous intervertebral discs, as shown in Figure 4. Different measurements were performed for each patient. Bone attenuation was evaluated both from children's head CT scans and from the phantom. In the first case, parietal skull bones from five children were considered; in the second case, ROIs were placed in the phantom vertebrae. The average HU of the simulated enchondromas was calculated from CT images of the inserts.

Obtained results will be displayed in Chapter 3 .

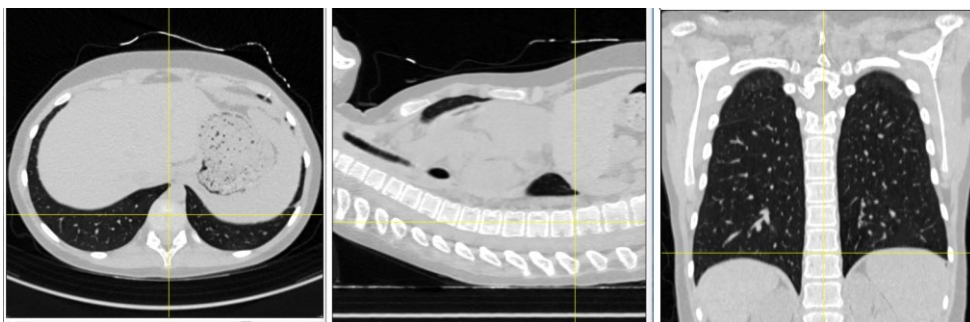


Figure 4 Example of cartilage HU evaluation. Coronal and sagittal views were used to locate intervertebral discs in the axial projections.

2.3.b. Phantom preparation

The inserts were randomly stuck on the 5-year-old anthropomorphic phantom anteriorly, posteriorly and laterally to simulate a real irregular arrangement of multiple enchondromas. The diameters of the inserts, measured with a caliper, ranged from 1.3 cm to 3.8 cm (shortest diameter) and from 2.0 to 4.9 cm (longest diameter).

Five different configurations were studied, changing each time the number and position of the inserts: in configurations A, B, C, D, and E, 16, 17, 3, 6, and 9 inserts were hung on the phantom, respectively.

2.3.c. Image acquisitions

The phantom was imaged at IRCCS Istituto Ortopedico Galeazzi. For each configuration, the phantom was irradiated using a CT scanner, a conventional radiography device and the EOS imaging system.

EOS imaging

The phantom was placed with vertical orientation in the scanning chamber, as shown in Figure 5. Laser-lights guides were used to properly center it. For every phantom configuration, three acquisitions were performed, changing each time the speed level:

- a) Speed level 2: 15.2 cm/s – total acquisition time = 4.26 s
- b) Speed level 3: 11.4 cm/s – total acquisition time = 6.39 s
- c) Speed level 4: 7.6 cm/s – total acquisition time = 8.53 s

The same current (200 mA) and tube potentials (83 kV and 102 kV for AP and LL projections, respectively) were automatically set for every acquisition. Obtained Dose-Area Product (DAP; mGy cm²) values are shown in Table 2.

Projection	Speed Level		
	2	3	4
AP	102.2	153.28	204.38
LL	156.41	234.61	312.81

Table 2 DAP values (mGy cm^2) of EOS AP and LL projections, acquired at three speed levels.

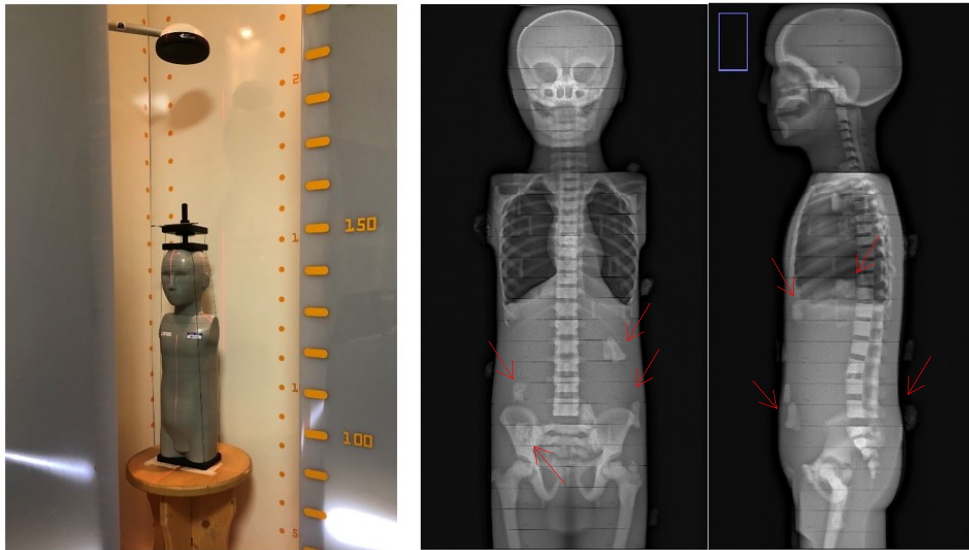


Figure 5 *Left*: Picture of EOS acquisition setup. The phantom was placed at the center of the scanning chamber and centered using laser-lights guides. The picture was taken before the inserts were hung on the phantom. *Right*: Examples of EOS AP and LL projections obtained with phantom configuration A. The red arrows indicate some of the enchondromas.

Digital Radiography

Acquisitions were performed with a modern Siemens Ysio Max X-ray system (Siemens AG, Erlangen, Germany) equipped with an automatic exposure control device. The phantom was positioned in horizontal orientation on the table, with the front directed toward the X-ray source. For LL acquisitions, it was rotated on the right side.

Depending on the scan range, the used acquisition protocol automatically divides the acquisition into two or three steps, with different tube angles.

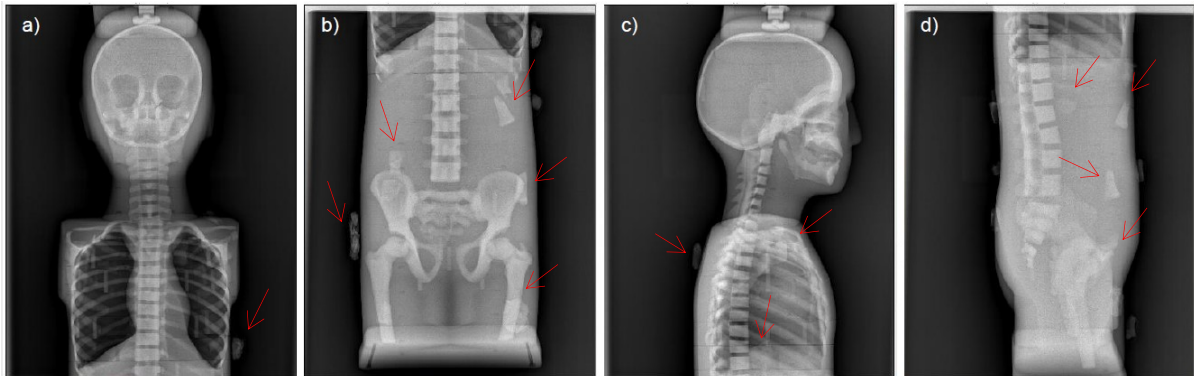


Figure 6 Examples of conventional radiographs for phantom configuration A. The red arrows indicate some of the enchondromas. a) AP projection of the upper body b) AP projection of the lower body; c) LL projection of the upper body and d) LL projection of the lower body.

Given the phantom dimensions, two scan regions – an upper from the top of the phantom to the diaphragm, and a lower from the diaphragm to the bottom of the phantom – were selected, as shown in Figure 6. Hence, two exposures were needed to capture the whole body; images were digitally stitched together post-acquisition to obtain whole-body AP and LL projections. The X-ray parameters reported in Table 3 were set automatically by the system. The same parameters were selected for each configuration of the phantom. The DAPs reported in Table 3 are computed as the average of values registered in the five acquisitions.

Projection	Parameter		
	kVp	mAs	DAP (mGy cm ²)
AP upper	74.8	8.8	282.0
AP lower	65.9	5.2	50.8
LL upper	74.8	2.1	163.7
LL lower	65.9	2.1	50.8

Table 3 Parameters of conventional radiography acquisitions. The same kVp and mAs were automatically set by the system for each phantom configuration. DAP values (mGy cm²) are computed as the average of those obtained in the acquisitions of the five configurations.

Computed Tomography

The phantom was positioned in the center of a modern 64-slice Siemens CT scanner (Definition AS+, Siemens Healthcare, Forchheim, Germany), as shown in Figure 7. CT examination was performed following indications of the Society for Pediatric Radiology [37].

Two topograms and a whole-body CT scan from head to feet were acquired for each configuration of the phantom. Image acquisitions parameters are reported in Table 4. Average $CTDI_{vol}$ and DLP were 5.69 mGy (range from 5.28 to 5.79 mGy) and 375.8 mGy cm (range from 367.8 to 384.3 mGy cm) respectively, with phantom size of 32 cm. The obtained $CTDI_{vol}$ meets the national DRL recommended for abdominal examinations [38]. Since the national and international DRLs [6,38] are stated only for exams of head, thorax, and abdomen, and not for whole-body examinations, no reference value was available for DLP.

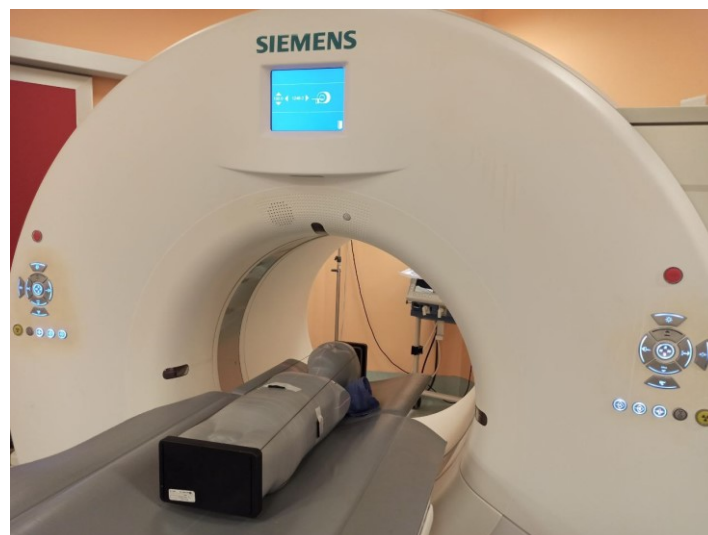


Figure 7 Acquisition of the phantom in computed tomography. The phantom was positioned in the center of the scanner using laser guides.

Two reconstruction kernels – b60 sharp and b20s smooth body spine - were applied.

Parameter	Topograms	Whole-body scan
Modality	Static	Spiral
mA	35	35
kV	120	120
Collimation	-	64x0.6
Slice thickness	0.6 mm	1 mm
Pitch	-	0.8
Care dose / Care kV	-	Active / Semi

Table 4 Acquisition parameters of topograms and whole-body scan.

2.3.d. Image quality analysis

Image quality analysis was performed in two steps. At first, two physicists (non-expert observers) reviewed the images. The visibility of enchondromas was evaluated by measuring their size using an electronic caliper.

Interobserver reliability was evaluated with Bland-Altman plot [39], a method extensively used to evaluate the agreement among two different observers or measurement techniques. The Bland-Altman plot displays the difference between the two techniques on the vertical axis, against the averages of the two techniques on the horizontal axis, allowing the identification of any systematic difference between the measurements (bias) or possible outliers. The mean difference is the estimated bias, and the standard deviation (SD) of the differences measures the random fluctuation around this mean. The limits of agreement (95% prediction interval) are calculated as the bias minus and plus 1.96 SD.

To evaluate interobserver variability, a slightly different approach was taken in the analysis of images from different modalities:

- Computed tomography: three dimensions were measured for every simulated enchondroma in each phantom configuration. Since CT images were reconstructed using two different algorithms, the impact

of the reconstruction kernel was evaluated. For this purpose, differences in the dimension of the inserts obtained in the two cases were calculated.

- EOS imaging system: four lengths were measured for each insert, two from AP and two from LL projections. The effect of speed level was investigated evaluating the differences in the computed dimensions.
- Conventional radiography: four measurements were performed for each insert, two from AP and two from LL projection. The reconstructed whole-body images were analyzed.

Then, a radiologist with five years of experience in musculoskeletal radiology and research and a resident radiologist examined the images. The results are proposed in the article of Albano et al. [26]. For the analysis, images were taken in random order and blinded to the number of inserts. The number of inserts visible on each image was counted and their size was measured. The longest length was considered for each insert and it was compared with the real dimension. Also in this case, the Bland-Altman method was applied to test interobserver and intermodality reproducibilities.

2.4. Revision of DR acquisition protocol

As introduced in Chapter 1, patients with Ollier disease often experience long follow-up, with multiple radiographs during childhood. Follow-up does not require the same level of image quality as that required for diagnosis, and a slight degradation of image quality can then be accepted in favor of dose reduction.

The EOS system provides the possibility to modify the speed level, a feature that can be fully exploited for follow-up purposes: indeed, as shown in Table 2, a 50% DAP reduction can be achieved by doubling the acquisition speed.

In digital radiography, the level of image quality and delivered dose can be managed through the manufacturer-dependent exposure index (EI) [40].

During this thesis work, the DR acquisition protocol described in the previous Chapter was optimized to be suitable for follow-up purposes. To do this, the EI of the Siemens system was varied trying to maintain comparable image quality. The acquisitions described in Section 2.3.c. - *Digital Radiography* were replicated with the new follow-up protocol, and images were analyzed in terms of in-phantom signal-difference-to-noise ratio (SdNR) to evaluate image quality degradation.

Since one of the purposes of this work was to test the visibility of cartilaginous structures, the bone of the phantom was considered for SdNR evaluations. Two ROIs were placed on a bone element and on a close uniform background region, on images acquired with both the original protocol suited for diagnosis and the new protocol optimized for follow-up. SdNR was evaluated as

$$\text{SdNR} = \frac{\text{PV}_{\text{bone}} - \text{PV}_{\text{bg}}}{\text{SD}_{\text{bg}}} \quad 1$$

where PV_{bone} and PV_{bg} are the mean values of the ROIs in the bone element and in the background region, respectively, and SD_{bg} is the standard deviation of the background ROI.

Since reconstructed AP and LL whole-body projections were analyzed in the evaluation of the system diagnostic performance, the same images were considered here. Results will be outlined in Section 3.3.

Table 5 summarized the DAP values (mGy cm^2) of AP and LL projections obtained with the two acquisition protocols.

Projection	kVp	DAP (mGy cm ²)	
		Diagnostic protocol	Follow-up protocol
AP upper	74.8	282	83.4
AP lower	65.9	50.8	65.3
LL upper	74.8	163.7	66.1
LL lower	65.9	50.8	65.2

Table 5 DAP (mGy cm²) and kVp of conventional radiography AP and LL projections obtained with the diagnostic and follow-up acquisition protocols.

2.5. Evaluation of dosimetric performance

2.5.a. Dosimetric simulations

Monte Carlo simulations were performed for each imaging technique. *PCXMC 2.0* was used to compute doses in conventional radiography and EOS, while *VirtualDose* was applied to calculate doses in computed tomography. The descriptions of the programs and details about the performed simulations are provided in the following Sections.

PCXMC 2.0

PCXMC (PC program for X-ray Monte Carlo) [41] is a MC software for computation of equivalent and effective doses in medical X-ray exposures. The calculation process consists of four main steps: setup definition, simulation process, dose calculation and risk assessment.

a) Set-up definition

First, the patient characteristics and the geometric setup have to be specified, as shown in Figure 8. In the present version (2.0) of the program, anatomical data are based on the mathematical hermaphrodite phantom models of Cristy and Eckermann [42], which describe patients of six different ages: newborn, 1, 5, 10, 15-year-old, adult male and adult female. Notwithstanding,

phantom weight and height can be modified to mimic patients of arbitrary size.

X-ray projections can be freely adjusted, by defining source distance, field size and position, and angles.

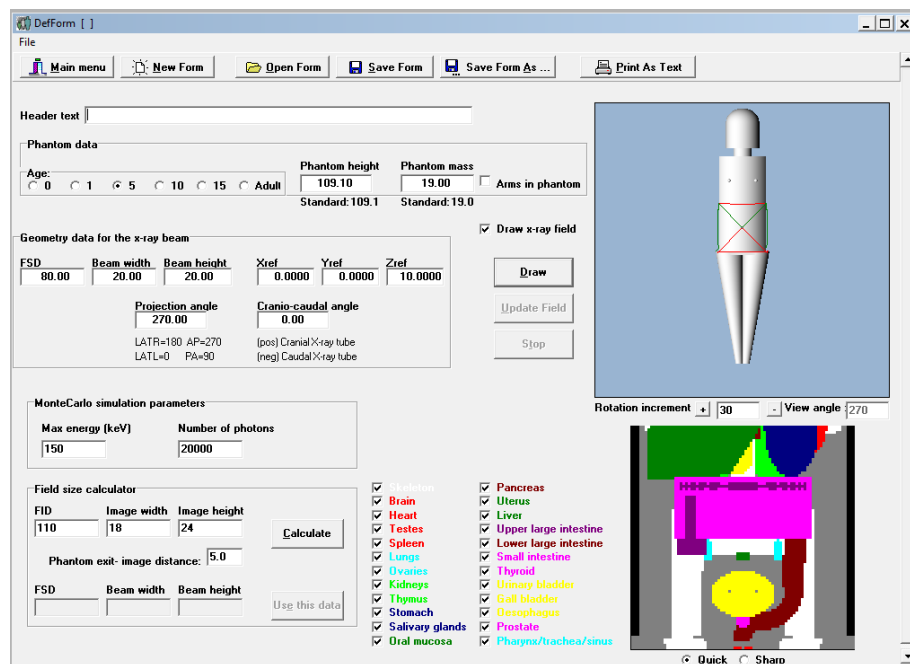


Figure 8 Definition of the geometric setup and patient characteristics in *PCXMC 2.0*.

b) Simulation process

The program simulates three physical interaction processes: photoelectric absorption, coherent Rayleigh scattering and Compton incoherent scattering. Photons are emitted from an isotropic point source into the solid angle defined by the geometric characteristics of the setup – focal distance and field dimensions - and randomly interact with the phantom, according to the probability distributions of the interaction processes. At each interaction point, energy deposition to the organ is computed and stored for subsequent dose calculation. The user can select the number of random independent histories, as well as the photons maximum energy. By default, 20000 photons

are generated. Estimates of the mean energy depositions in the various tissues and organs are used for calculating the corresponding doses.

c) Dose calculation

The third step concerns dose calculation. Active bone marrow, adrenals, brain, breasts, colon (upper and lower large intestine), extrathoracic airways, gallbladder, heart, kidneys, liver, lungs, lymph nodes, muscle, oesophagus, oral mucosa, ovaries, pancreas, prostate, salivary glands, skeleton, skin, small intestine, spleen, stomach, testicles, thymus, thyroid, urinary bladder and uterus are considered for organ dose calculations.

Organ doses are given in proportion to the incident air kerma, which have to be supplied by the user. Alternatively, the program supports exposure, air kerma-area product and exposure-area product. To compute conversion factors from air kerma to tissue dose, characteristics of the energy spectrum (X-ray tube voltage, tube current-time product, total filtration and focal spot-to-skin distance) have to be specified. In addition to organ doses, the program calculates effective dose, using both the tissue weighting factors of ICRP Publication 103 [43] and of ICRP Publication 60 [2].

d) Risk assessment

Calculated organ doses can be used for the assessment of the risk of radiation-induced cancer. Risk models derived by BEIR VII committee [44] are applied in the program. BEIR does not provide risk estimates for all organs and tissues. For organs that are not included in the risk models, *PCXMC 2.0* estimates the risk of cancer death using BEIR's model for "other solid cancers". Three different quantities are used to assess lifetime risks, namely risk of exposure-induced death (REID), loss of life expectancy (LLE) and loss of life expectancy per radiation-induced fatal cancer (LLE/REID).

Virtual Dose

VirtualDose (Virtual Phantoms Inc.; Albany, New York) is a web-based software for reporting organ doses to patients undergoing diagnostic CT examinations [45], and it is provided at our institution within the Radiation Dose Index Monitoring (RDIM) software EmmeEsse *Physico* (EMME ESSE M.S. SRL; Milan; Italy). The program is based on a comprehensive database of organ doses derived from MC simulations, involving a library of 25 anatomically realistic phantoms and 2 validated CT scanners. The 25 whole-body voxel phantoms include reference adults (male and female), pediatric patients at different ages (newborn, 1, 5, 10 and 15 year-old), pregnant females at three gestational stages (pregnant 3, 6 and 9 months) and a newly developed set of phantoms representing overweight and obese patients. GE LightSpeed Pro 16 and Siemens SOMATOM Sensation 16 are constructed in the MC code. For CT scanners other than the two explicitly validated in the software, correction factors can be calculated from the measured $CTDI_{vol}$, so that nearly any modern CT scanner can be represented.

To compute organ doses, the program first deconstructs the scan range into the individual tube rotations. A series of separate axial scans from head to toe is then simulated. For each simulated slice, the direct dose within the scan volume and the scattered radiation outside of the scan are calculated. Once the axial slice-by-slice dose database has been established, organ doses from a contiguous axial scan are obtained by directly summing the corresponding single axial contributions. For non-contiguous (pitch > 1) or overlapping (pitch < 1) helical scans, radiation dose is rescaled inversely proportionally to the pitch value.

VirtualDose provides an interactive graphical user interface, composed of three different layers: a parameter selection panel, a patient model/scan range display, and a dose result display. The parameter selection panel

provides the options for a user to specify the operating conditions of a particular CT scan. The available input features include phantom type, CT scanner manufacturer and model, X-ray tube voltage, beam collimation, tube current-time product, pitch specification, CTDI_{vol}, and protocol anatomical region. The software has the option to read the parameters from the DICOM file header or from the DICOM object Radiation Dose Structured Report (RDSR). If some parameters are not available from a DICOM file, the program will select default values automatically and users are allowed to change them, as shown in Figure 9.

Peso (kg)	<input type="text"/>
Altezza (m)	1.64
Sesso	M
Età	78
Distretto	CHEST <input type="button" value="v"/>
Fantoccio	Adult Male-50th Percentile <input type="button" value="v"/>
Ct Vendor	Siemens
Ct Model	Siemens Definition Flash(Flash mode)
Kv	80
mAs	132.87
Collimazione	38.4
CTDI	3.81
Pitch	0.9
Scansione(cm)	13.8
Diametro Efficace(cm)	30.6 <input type="checkbox"/> Escludi

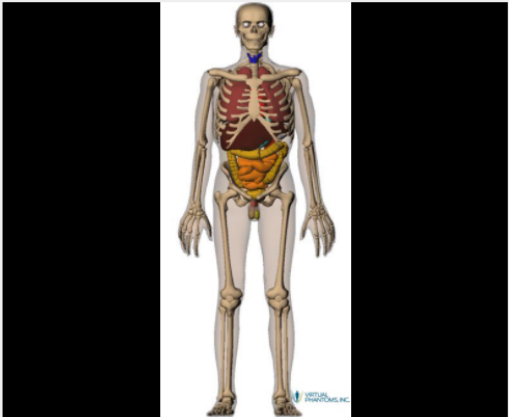


Figure 9 *VirtualDose* parameter selection panel within the RDIM platform. Parameters are read from the DICOM file. Features not available in the DICOM objects (weight, height, anatomical region and phantom type) can be selected by the user.

Scan range is automatically set based on the selected CT protocol. The user can accept default coverage or adjust it.

Based on the user-specified scan parameters, *VirtualDose* fetches and calculates the patient-specific organ dose data from the remote server-side database.

Simulation of EOS acquisitions

Different approaches can be found in the literature regarding the simulation of slot-scanning EOS acquisitions. Law et al. [16,46] divided the scan range in contiguous 0.5 mm-high slot beams and performed different simulations across the whole spine. Organ doses were then computed as the sum of single-beam contributions. Hui et al. [19], instead, performed only one simulation, selecting field dimensions to include the full body. Since the continuous scanning of EOS imaging technique consists of one single shot radiation exposure, and the system provides a single DAP value for each projection, the approach of Hui et al was applied in this work. However, to avoid the effect of beam divergence, an infinite focus-to-skin (FSD) distance (actually 100 m) was selected. For comparison, simulations were also performed at a fixed FSD.

AP and LL projections were separately simulated. For each speed level, organ doses were computed by the sum of the two contributions. Table 6 shows the set up and geometrical simulation parameters. Since the phantom is not provided with arms, also the simulations were performed with no arms.

Parameter	Value
Phantom data	5-year (height 110 cm, weight 19 kg); no Arms in phantom
FSD [cm]	1000 (infinite)
Beam dimensions [cm]	44.8 width; 65 height
(Xref, Yref, Zref)	(0, 0, 27.5)
Projection angle [degree]	<ul style="list-style-type: none"> • AP projection: 270 • LL projection: 0
Cranio-caudal angle [degree]	0

Table 6 Setup parameters used for *PCXMC* simulations of EOS acquisitions. Parameters were selected to reproduce experimental acquisitions described in Section 2.3.c.

The AP projection field, as displayed in the *PCXMC* interface, is shown in Figure 10.



Figure 10 *PCXMC 2.0* interface: representation of AP projection field in EOS acquisitions.

50000 photons were generated in each simulation, setting a maximum energy of 150 keV. Two energy spectra were generated: according to acquisition parameters described in Section 2.3.c. - *EOS imaging*, tube peak potentials of 83 kVp and 102 kVp were selected for AP and LL projections, respectively. Based on the results of manufacturer annual tests, the X-ray beam quality was simulated with a total filtration of 3.5 mm aluminum (Al) + 0.1 mm copper (Cu). DAP values reported in Table 2 were provided as input dose quantities.

Simulation of digital radiography acquisitions

Both the acquisitions performed with the diagnostic protocol (see Section 2.3.c. *Digital Radiography*) and with the follow-up protocol (see Section 2.4.), were simulated. Since the acquisition geometry was identical, the same patient and setup parameters, reported in Table 7, were selected in the two cases. AP and LL projections of the upper and lower body regions were separately simulated and organ doses were computed by the sum of the four contributions.

Parameter	Projection			
	AP upper	AP lower	LL upper	LL lower
Phantom	5-year	5-year	5-year	5-year
Height [cm]	110	110	110	110
Mass [kg]	19	19	19	19
Arms in phantom	no	no	no	no
Focus to skin distance [cm]	117.2	117.2	117.2	117.2
Focus to image distance [cm]	130.3	130.3	130.3	130.3
Beam width [cm]	27.36	27.36	27.36	27.36
Beam height [cm]	35.01	35.01	35.01	35.01
(Xref, Yref, Zref)	(0, 0, 42)	(0, 0, 10)	(0, 0, 42)	(0, 0, 10)
Projection angle [degree]	270	270	0	0
Cranio-caudal angle [degree]	0	0	0	0

Table 7 Setup parameters used for *PCXMC* simulations of DR acquisitions. *Upper* and *Lower* refer to acquisitions of the upper and lower body regions. Parameters were selected to reproduce experimental acquisitions described in Section 2.3.c.

50000 photons were generated in each simulation, setting a maximum energy of 150 keV. Different energy spectra were generated for acquisitions of upper and lower regions: according to Table 3 and Table 5, tube peak potentials of 75 kVp and 66 kVp were selected, respectively, with total filtration of 2.8 mm Al equivalent.

DAP values reported in Table 3 and in Table 5 were provided as input dose quantities for the simulation of examinations performed with the diagnostic and the follow-up protocols, respectively.

Simulation of computed tomography acquisitions

The CT acquisition described in Section 2.3.c. - *Computed Tomography* was simulated using *VirtualDose*. The software read the acquisition parameters from the DICOM RDSR provided within the RDIM software *Physico*. CT vendor and model, kV, mAs, collimation, $CTDI_{vol}$, pitch and scan length were automatically set. A 5-year-old-male phantom (weight 19 kg, height 110 cm)

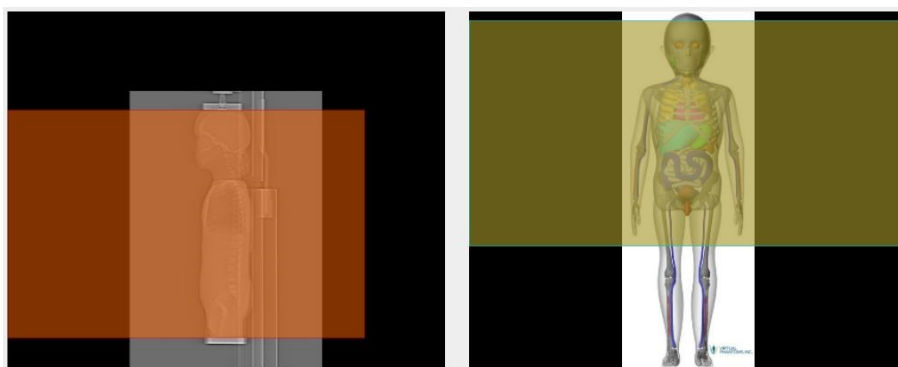


Figure 11 Definition of the scan geometry within the *VirtualDose* software. The scan range is defined on the topograms and projected on the selected phantom.

was manually selected. The *Manual Scan Range* option was exploited to optimize the scan range selection: as shown in Figure 11, this feature allows to manually define the coverage region based on the acquired topograms.

2.5.b. Dosimetric measurements

Different MC software was used to simulate CT, EOS, and DR acquisitions. While the application of *PCXMC* for organ dose assessment in digital radiography has been already validated [47–49], to our knowledge there are no comprehensive studies for EOS. Different authors [16,17,19,46] performed MC simulations, but their results were not validated with experimental measurements. This is of major concern because the software was developed to simulate conventional radiography acquisitions and not the slot-scanning EOS acquisitions. Then, to validate the results of simulations,

doses to some organs of interest were also assessed with in-phantom measurements with TLDs. For completeness, experimental measurements were performed also for DR and CT.

The characterization and calibration of dosimeters, the phantom acquisition, and the performed analysis are described in the following Paragraphs.

Characterization and calibration of dosimeters

Thermoluminescent dosimeters type GR-200A

In this study TLDs type GR-200A - lithium fluoride materials doped with Magnesium, Copper and Phosphorus (LiF:Mg, Cu, P) – were employed. They are chips round in shape (diameter 4.5 mm; thickness 0.8 mm) suited for the placement in the CIRS ATOM dosimetry phantom.

Main advantages of LiF:Mg, Cu, P GR 200A TL dosimeters include a very high sensitivity, a good reproducibility of readouts, low detection threshold (of a fraction of μGy) and no appreciable fading within six months.

TLD characterization

Repeatability and linearity of the dosimeters were investigated with experimental measurements.

Repeatability was evaluated to quantify the uncertainty of TLDs response. For this purpose, a batch of dosimeters was exposed five times to the same irradiation dose with a TLD irradiator (DoseRad II V1 R2, EL.SE. s.r.l., Milan, Italy), and subsequently read out with a RADOS-RE 2000 reader (RadPro International GmbH, Schwanen, Germany). Measurements were repeated for two irradiation doses: 250 μGy , which was the minimum achievable value, and 1.7 mGy. For each TLD, repeatability was quantified as the coefficient of variation (CV) of the measurements, as shown in Equation 2.

$$CV (\%) = \frac{SD}{mean} \quad 2$$

where *SD* and *mean* are the standard deviation and the mean value among different measurements, respectively.

Moreover, since high doses were expected in CT acquisitions, linearity was investigated. For this purpose, TLDs were irradiated at different doses from 250 μ Gy to 28 mGy. The relationship between the average response and the irradiation dose was investigated.

TLD calibration

TLDs were calibrated in air in the range of kVp used in the study. Different calibration curves were calculated to investigate the possible energy dependence in the response of TLDs. Indeed, the quality of the X-rays beam absorbed by the TLD within the phantom might differ from the quality of the generated beam, due to the phantom attenuation and, for DR imaging, due to the position with respect to the radiation field. Thus, if the TLD response changes with the energy, a proper calibration curve has to be applied. The X-ray energy spectrum modification was first investigated.

For this purpose, a Philips OmniDiagnost Eleva device was used under reproducible conditions. Measurements were performed at a fixed source-to-detector distance of 100 cm with a RaySafe X2 dosimeter (RaySafe, Billdal, Sweden) with calibration traceable to national standards. Different measurements were performed selecting fixed source energy and source-to-detector distance and varying the thickness of PMMA above the dosimeter. The variation of the X-ray energy spectrum due to PMMA attenuation produced a change in the half-value layer (HVL) and peak kilovoltage (kVp) measured by the dosimeter. Two different source kVp, 80 and 120, were considered.

Based on the obtained results, calibration curves at 66 kVp and 75 kVp were calculated for dose measurements in digital radiography; curves at 82 kVp, 97 kVp, and 102 kVp were computed for measurements in EOS and curves at 110 kVp, and 120 kVp were evaluated for computed tomography. This choice will be fully explained in Section 3.4.a. For each imaging technique, the dose range was determined based on the results of dosimetric simulations. Although X-ray beam quality of EOS, CT and DR systems are different, the same Philips OmniDiagnost Eleva DR device was used for TLD calibration. Indeed, measurements could not be performed with the EOS system due to its scanning nature and with the CT scanner due to impossibility to reach low doses. To guarantee the same exposure and backscattering conditions, TLDs were placed side-by-side with the dosimeter on a Styrofoam support, properly designed so that the chamber and TLD crystals were at the same distance from the source.

Five measurements were performed for each calibration curve, exposing three TLDs to each dose. Two cards were used to estimate the background radiation.

Phantom acquisition

The phantom was filled with dosimeters from bottom up using a vacuum pump. Seventy-five TLDs were employed. Two cards were used to evaluate background radiation. TLDs were positioned in the most radiosensitive organs, as reported in Table 8, with guidance from a human anatomy CT atlas. To allow the placement of the dosimeters, the selected holes were filled with cut plugs (See Section 2.2.). Each TLD was identified with the number of the card, followed by a progressive number from 1 to 3, and subsequently associated with the unique hole ID. Unused holes were filled with tissue

equivalent uncut plugs. To evaluate skin dose, four cards were placed on the phantom surface, anteriorly, posteriorly, and on the right and left sides.

Organ	Number of detector holes	Organ	Number of detector holes
Eyes	2	Pancreas	2
Brain	4	Kidneys	4
Thyroid	2	Intestine	8
Heart	2	Urinary Bladder	2
Lungs	6	Testes	2
Liver	8	Prostate	1
Esophagus	3	Breasts	2
Stomach	4	Skin*	12
Active bone marrow	11		

Table 8 List of the organs investigated with dosimetric in-phantom measurements; for each organ, the number of employed TLDs is reported. *For skin dose evaluation four cards were placed on the phantom surface.

The phantom was imaged with CT, DR, and EOS at three different speed levels. For EOS and CT the setup and acquisition parameters described in Section 2.3.c. were replicated. DR acquisitions were performed with the low-dose protocol for follow-up described in Section 2.4.

Based on MC simulations, doses of 30-40 μGy were expected for some organs in DR and EOS acquisitions. Since the accuracy of the response of TLDs could not be tested for such low doses, in order to accumulate a sufficient dose the EOS and DR irradiations were repeated three times. A similar approach was taken by Damet et al. [8] and Pedersen et al. [10]. Obtained results were then normalized to a single examination. Organ doses of about 10 mSv were instead obtained from the simulations of CT acquisitions. Thus, only one irradiation was performed for CT.

After each irradiation, the dosimeters were removed from the top down and read out. To take into account possible variations of the patient position and

of exposure parameters in different examinations, for each imaging technique the experiment was repeated three times.

Organ dose calculation

TLD responses were individually corrected for individual sensitivity and background radiation. For each position inside the phantom, the average value and the standard deviations among the three measurements were then calculated. Organ doses were computed applying to the TLD average response a proper calibration curve, as in Equation 3

$$D \text{ (mSv)} = S_{\text{TLD}} \cdot m_{\text{cal}} + q_{\text{cal}}, \quad 3$$

where S_{TLD} , m_{cal} , and q_{cal} refer to TLD signal, and calibration curve slope and intercept, respectively.

A different approach was taken for different imaging techniques:

- EOS imaging system

AP and LL projections were acquired with 83 kVp and 102 kVp, respectively. Thus, to better reproduce this acquisition setup, two calibration curves were applied to the response of each TLD, computing separately the dose contributions derived from AP and LL projections. The final dose was calculated as the weighted sum of the two, using the ratio of DAP values in the two projections as a weighting factor.

- Conventional radiography

Different kVp were selected for radiographs of the upper and lower part of the phantom. For this reason, different calibration curves were applied to TLDs placed in holes from head to diaphragm, and from diaphragm to legs.

- Computed tomography

The CT scan was performed without kV modulation. A unique calibration curve was then applied.

Further considerations about the choice of calibration curves will be provided in Section 3.4.b.

The dose error was computed applying the theory of propagation of uncertainty, starting from the statistical uncertainties of the TLD signal, curve slope, and curve intercept, as reported in Equation 4.

$$\sigma_D = \sqrt{\sum_i \left(\frac{\partial D}{\partial i}\right)^2 \sigma_i^2} = \sqrt{S_{TLD}^2 \sigma_m^2 + m^2 \sigma_{S_{TLD}}^2 + \sigma_q^2} \quad 4$$

For organs for which more than one TLD was used, the mean value was calculated. It is worth noting that especially for DR and EOS, a large variation in the response of different TLDs was expected for some organs. For instance for lungs, breasts, and eyes, a higher dose was expected for the organ on the left of the body, which was closer to the X-ray source in LL acquisitions, with respect to the right organ. For this reason, when more than one TLD was involved, the dose uncertainty was not computed as the standard deviation of the measurements but applying the theory of propagation of uncertainty.

2.5.c. Effective dose and risk computation

Effective doses (E) were provided both by *PCXMC* for DR and EOS and by *VirtualDose* for CT. For each imaging technique it was also calculated according to ICRP 103 recommendations [43], as the sum

$$E = \sum_T W_T \sum_R W_R D_{T,R} \quad 5$$

where W_R is the radiation weighting factor (being unity for X-rays), $D_{T,R}$ is the absorbed dose to an organ or tissue measured with TLDs, and W_T is the tissue weighting factor. Tissue weighting factors recommended by ICRP 103, and

reported in Table 9, were applied. Doses to oral mucosa, intestine, and active bone marrow were assumed attributable to dose to salivary glands, colon, and bone surface, respectively; dose to remainder tissues was computed as the average of doses to heart, kidneys, oral mucosa, pancreas, prostate, and intestine. The uncertainty of effective dose was evaluated from the errors of $D_{T,R}$ through the propagation of uncertainties.

Organ/Tissue	W_T
Red bone marrow, colon, lung, stomach, breast, remainder tissues	0.12
Gonads	0.08
Bladder, oesophagus, liver, thyroid	0.04
Bone surface, brain, salivary glands, skin	0.01

Table 9 Tissue weighting factors recommended by ICRP 103. For a male patient, remainder tissues include adrenals, extrathoracic region, gallbladder, heart, kidneys, lymphatic nodes, muscle, oral mucosa, pancreas, prostate, small intestine, spleen, and thymus.

The effective doses were used to estimate risks of radiation-induced cancer for each imaging technique. The risk was computed with the methods introduced in the Biological Effects of Ionizing Radiation (BEIR) VII report [44] and in the Public Health England (HPA) studies [50] in the form of LAR (Life Attributable Risk) of cancer incidence. LAR is defined as the excess probability of developing cancer after exposure and it depends on the age at exposure, gender, and population. In this study, the risk due to a single uniform whole-body examination performed during childhood was estimated. Nominal risk coefficients for a 5-year-old patient were used for BEIR VII, while the range 0-9 years was selected for estimations with the HPA method. Males and females were separately considered. Despite the 5-year-old phantom representing a male child, the calculated effective dose was used also for risk estimation in females. For comparison, LAR was computed also with the nominal risk coefficient of ICRP 103 [43].

Chapter 3 Results

3.1. Preliminary study: simulation of enchondromas

Figure 12 compares the measured average HU of pediatric cartilage (red) and bone (green), phantom bone (blue) and simulated enchondromas (orange). Numerical values are reported in Table 10. Errors are computed as the standard deviation among different measurements.

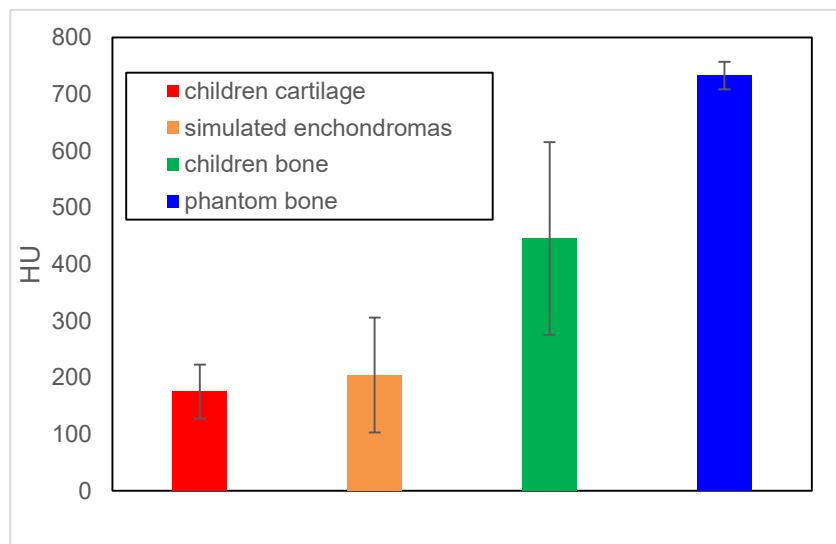


Figure 12 Average Hounsfield Units of children cartilage (red), Ollier simulated enchondromas (orange), children bone (green) and phantom bone (blue). Error bars represent \pm one standard deviation.

Tissue	Measured HU
Simulated enchondromas	204 \pm 101
Children cartilage	175 \pm 47
Children bone	445 \pm 170
Phantom bone	732 \pm 24

Table 10 Measured average HUs of simulated enchondromas, pediatric cartilage and bone, and phantom bone. The reported error represents one standard deviation.

A good agreement was found between the simulated enchondromas and the pediatric cartilage, with a relative difference in measured HU of 14%. Considerably higher attenuation were measured for pediatric bone and phantom bone.

A smaller error was obtained for phantom bone, compared to the other elements. This was due to the high homogeneity of the tissue. Uncertainties of pediatric cartilage and bone were instead affected by interindividual variability. Finally, the high uncertainty of simulated enchondromas was due to the heterogeneity of the tissue, which is made of chicken bone, cartilage, fibrotic tissue, and air.

3.2. Image quality evaluation

3.2.a. Non-expert observers analysis

Analysis of CT images

All the inserts were perfectly visible in each phantom configuration. The Bland-Altman plot in Figure 13 shows the differences in diameters measured from CT images reconstructed with b60 sharp reconstruction kernel by the two observers. A bias of -0.55 mm (95% prediction interval from -2.6 mm to 1.5 mm) was recorded.

Similar results (bias -0.75 mm; 95% prediction interval from -2.67 mm to 1.17 mm) were obtained from images reconstructed with b20 smooth kernel. To evaluate the impact of the reconstruction algorithm, diameters obtained in the two cases were compared. A perfect agreement (median difference of 0.42 mm; range [-4.30 mm; 3.77 mm]) was observed.

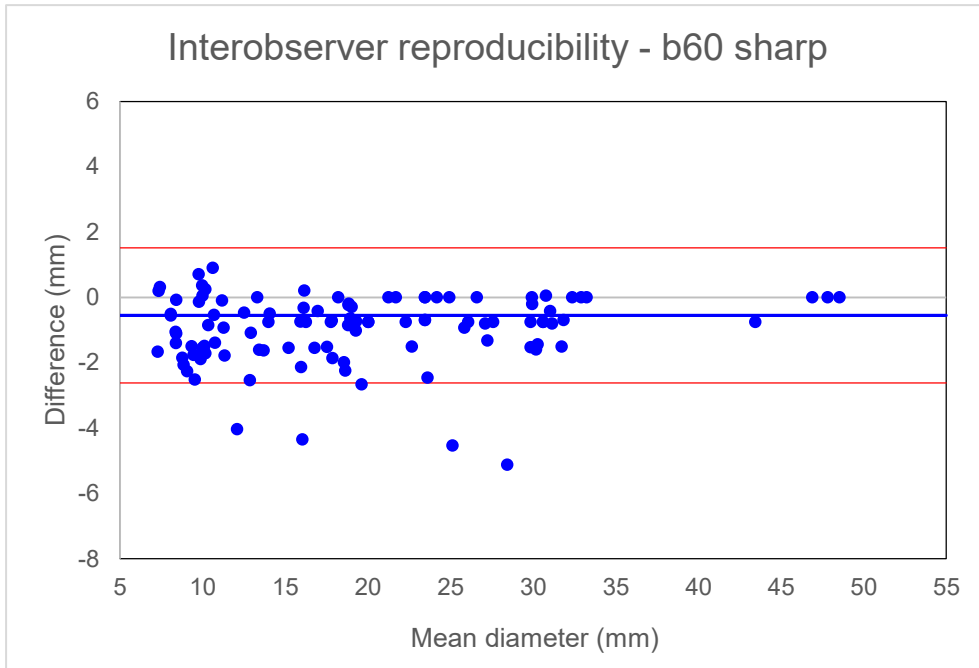


Figure 13 Interobserver reproducibility in computed tomography. The mean of the measured lengths is reported on the x-axis; the difference is reported on the y-axis. The blue line corresponds to the bias. The red lines define the limits of agreement.

Analysis of EOS images

The two observers were able to detect all the inserts placed on the phantom in each configuration. However, in some cases they were identified only in one projection. The Bland-Altman plot in Figure 14 shows the differences in diameters measured by the two observers from EOS projections acquired with the fast protocol (speed level 2). A bias of -0.76 mm (95% prediction interval from -6.6 mm to 5.1 mm) was recorded.

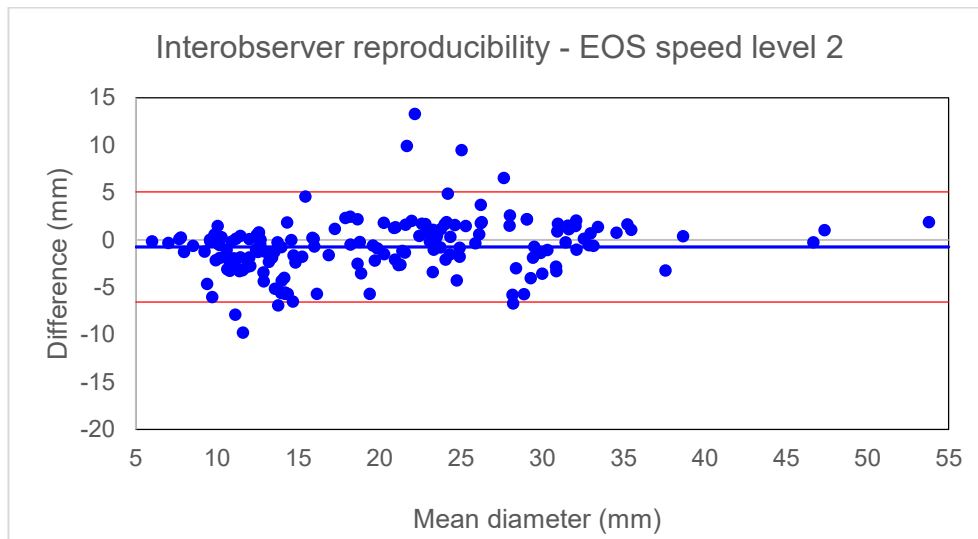


Figure 14 Interobserver reproducibility in EOS acquisitions at speed level 2. The mean of the measured lengths is reported on the x-axis; the difference is reported on the y-axis. The blue line corresponds to the bias. The red lines define the limits of agreement.

Similar results (bias -0.54 mm; 95% prediction interval from -7.6 mm to 6.5 mm, and bias -0.47; 95% prediction interval from -8.2 mm to 7.2 mm) were obtained from images acquired at speed levels 2 and 3, respectively. To evaluate the impact of the speed level, diameters obtained in the three cases were compared. Negligible variation (median difference of 0.06 mm; range [-6.78 mm; 6.38 mm]) was obtained.

Analysis of conventional radiography projections

The two observers were able to detect all the inserts placed on the phantom in each configuration. However, in some cases they were identified only in one projection. The Bland-Altman plot in Figure 15 shows the differences in diameters measured by the two observers from conventional radiography projections. A bias of -0.74 mm (95% prediction interval from -7.7 mm to 6.2 mm) was recorded.

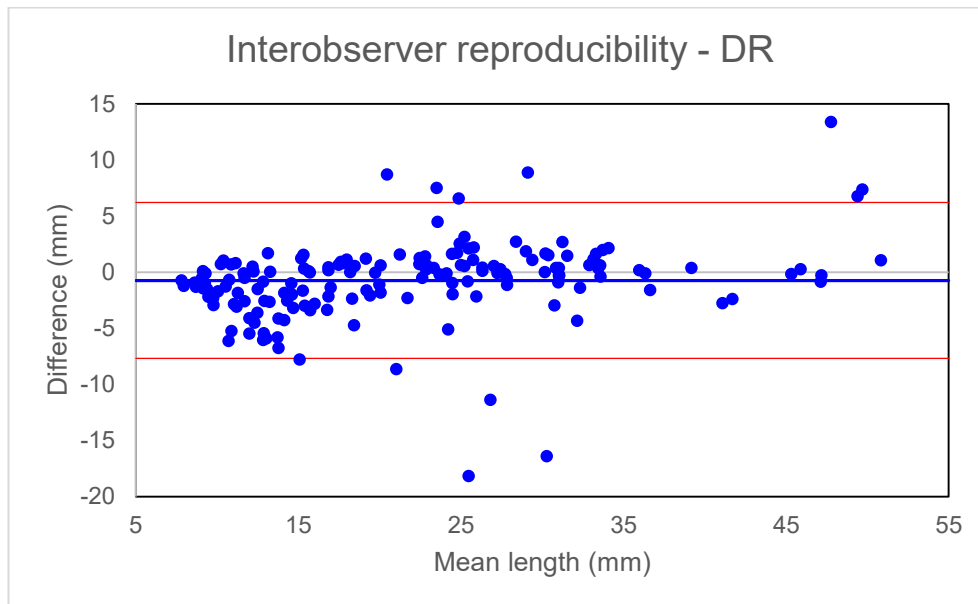


Figure 15 Interobserver reproducibility in conventional radiography. The mean of the measured lengths is displayed on the x-axis; the difference is reported on the y-axis. The blue line corresponds to the bias. The red lines define the limits of agreement.

3.2.b. Analysis of expert observers

The results outlined in the previous Section show no image quality variation with the reconstruction algorithm in CT, and the acquisition speed in EOS. For this reason, the radiologists analyzed only CT scans reconstructed with b60 sharp kernel and EOS images acquired with the fast protocol. Images were reviewed in random order and blinded to the number of inserts.

Both observers were able to detect the same number of inserts on EOS, DR, and CT. This was equal to the number of inserts placed on the phantom in 4/5 configurations for EOS and DR. In configuration B, 1 out of 17 inserts was not distinguished. On CT images, instead, the correct number of inserts was always detected.

To compare the performances of different imaging modalities, the longest length was measured for each insert. Intermodality reliability was quantified as Bland-Altman bias. Excellent agreement was obtained: bias of 0.14 mm

(88% reproducibility; 95% prediction interval from -2.8 to 3.1) and 0.15 mm (81% reproducibility; 95% prediction interval from -5.5 to 5.2 mm) were found when comparing EOS to DR and CT, respectively. It is worth noting that image pixel sizes of DR and EOS were equal to 0.13 mm and 0.18 mm, respectively, while CT voxel size was equal to 0.56x0.56x0.82 mm³.

Results are shown in Bland-Altman plots in Figure 16.

The size of the inserts measured from DR and EOS images was also compared with the real dimensions. Both techniques underestimated the true length by an average of 6.6 mm for DR (range from -19 mm to +2 mm) and 6.1 mm for EOS (range from -18 mm to +1 mm). Average relative magnifications, derived by dividing the difference between the measured length and the true length by the true length, of -23.9% (EOS) and -25.2% (DR) were obtained.

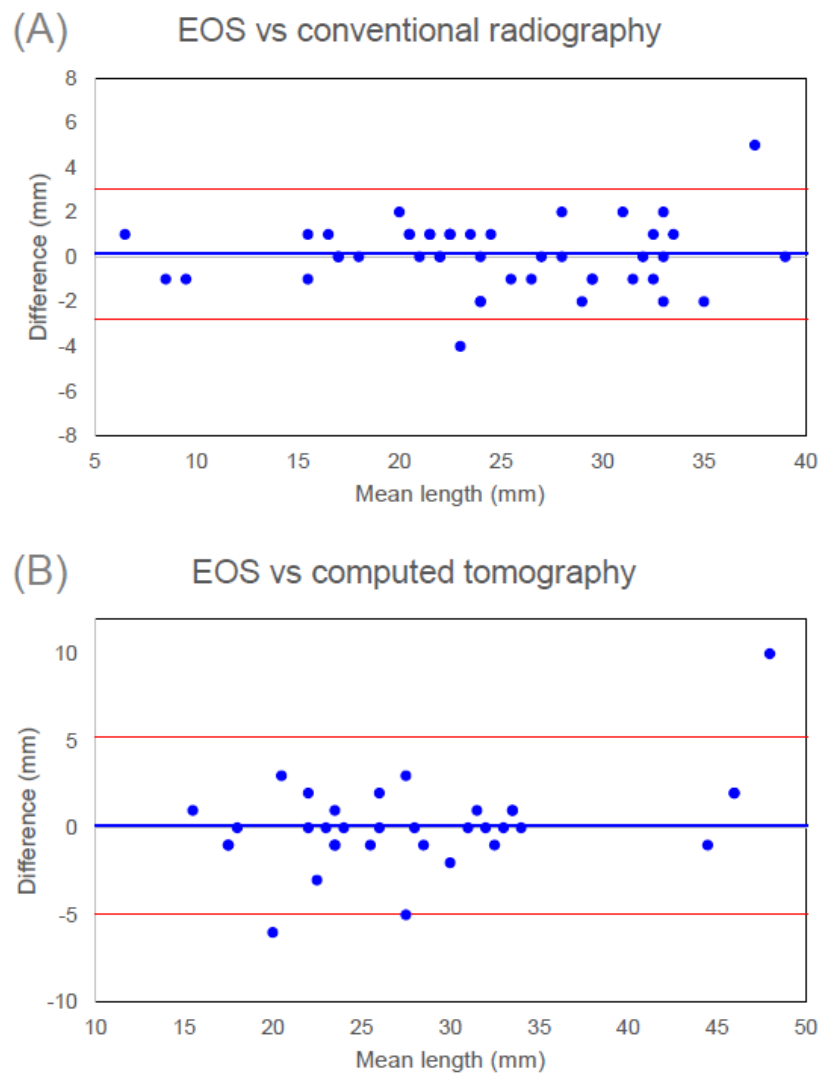


Figure 16 Intermodality reliability of insert length measurements among (A) EOS and DR, and (B) EOS and CT. The mean of the lengths measured from different techniques is displayed on the x-axis; the difference is reported on the y-axis. The blue line corresponds to the bias. The red lines define the limits of agreement.

3.3. Analysis of the DR acquisition protocol optimized for follow-up

In Figure 17 the DAP values of DR acquisitions performed with the diagnostic and follow-up protocols are compared. Considerable reduction was observed in DAP of both AP and LL projections of the upper body, while slight increases were observed for projections of the lower body. Total DAP of 547.3 mGy cm² and 280.0 mGy cm² were obtained for the diagnostic and follow-up acquisition protocols, which correspond to a reduction of 49%.

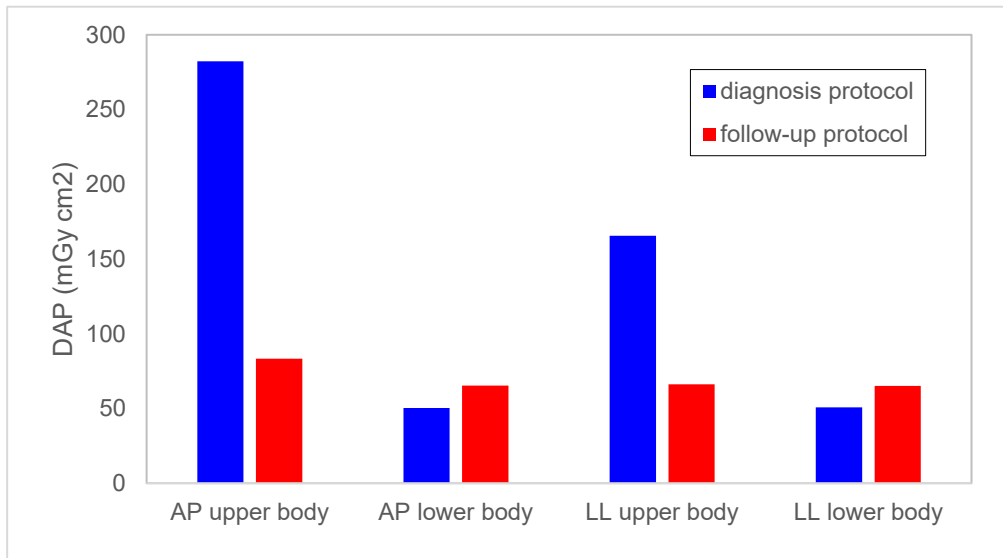


Figure 17 Comparison of DAP values (mGy cm²) in AP and LL projections of DR acquisitions performed with the diagnostic (blue) and follow-up (red) protocols.

To evaluate SdNR, bone structures surrounded by a homogeneous background were needed. Eight elements were identified, four in AP projection (two lumbar vertebrae, the hip bone, and the right femur), and four in LL projection (the skull, a cervical vertebrae, and two lumbar vertebrae). The position of the ROIs is shown in Figure 18. The outcomes are reported in Table 11. Average and median reductions in SdNR of 4% and 1% (range from -23% to 9%) were measured with the follow-up protocol.

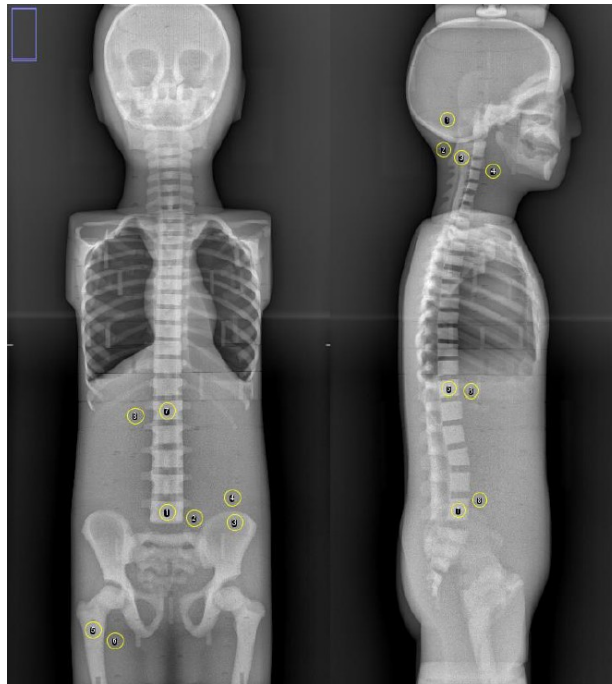


Figure 18 Position of the ROIs for SdNR evaluation. Two ROIs were considered for each measurement, one placed inside the bone structure, and the other on an adjacent background region.

Projection	element position	SdNR	
		Follow-up protocol	diagnosis protocol
AP	lumbar vertebrae (bottom)	4.4	4.0
AP	hip bone	1.9	1.9
AP	femur	7.9	7.4
AP	lumbar vertebrae (top)	3.1	2.9
LL	skull	6.6	6.6
LL	cervical vertebra	6.3	7.5
LL	lumbar vertebrae (top)	2.6	3.3
LL	lumbar vertebrae (bottom)	2.9	3.3

Table 11 SdNR of bone elements evaluated from DR images obtained with the follow-up and the diagnosis acquisition protocols.

3.4. Assessment of dosimetric performance

3.4.a. Monte Carlo simulations

Simulation of EOS acquisitions

Figure 19, and Figure 20 compare organ doses in EOS acquisitions at speed levels 2, 3, and 4, obtained for finite (blue) and infinite (red) focus-to-skin distance. For each acquisition speed, doses calculated with infinite FSD were higher than those calculated with finite distance for almost all organs, with the exception of breasts. Differences ranged from -27% (for breasts) to $+39\%$ (for prostate), with a median value of 7% . For 12 out of 17 organs (71%) error bars overlapped, indicating no statistically significant differences.

Effective doses, computed by *PCXMC* with both ICRP 60 and ICRP 103 tissue weighting factors, are listed in Table 12. A relative reduction of effective dose of 33% and 50% was observed with the fast acquisition protocol (speed level 2) with respect to speed levels 3 and 4, respectively.

	FSD	Effective Dose (μSv)	
		ICRP 60	ICRP 103
Speed Level 2	Finite	64.0 ± 2.6	68.0 ± 2.8
	Infinite	68.9 ± 2.6	70.6 ± 2.8
Speed Level 3	Finite	96.0 ± 3.8	102.1 ± 4.4
	Infinite	103.4 ± 3.8	105.9 ± 4.2
Speed Level 4	Finite	128.1 ± 5.3	136.1 ± 5.8
	Infinite	137.9 ± 5.0	141.2 ± 5.6

Table 12 Effective doses (μSv) computed by *PCXMC* for EOS acquisitions at different speed levels, with finite and infinite FSD. Results obtained with both ICRP 60 and ICRP 103 tissue weighting factors are reported. Errors refer to 2 standard deviations.

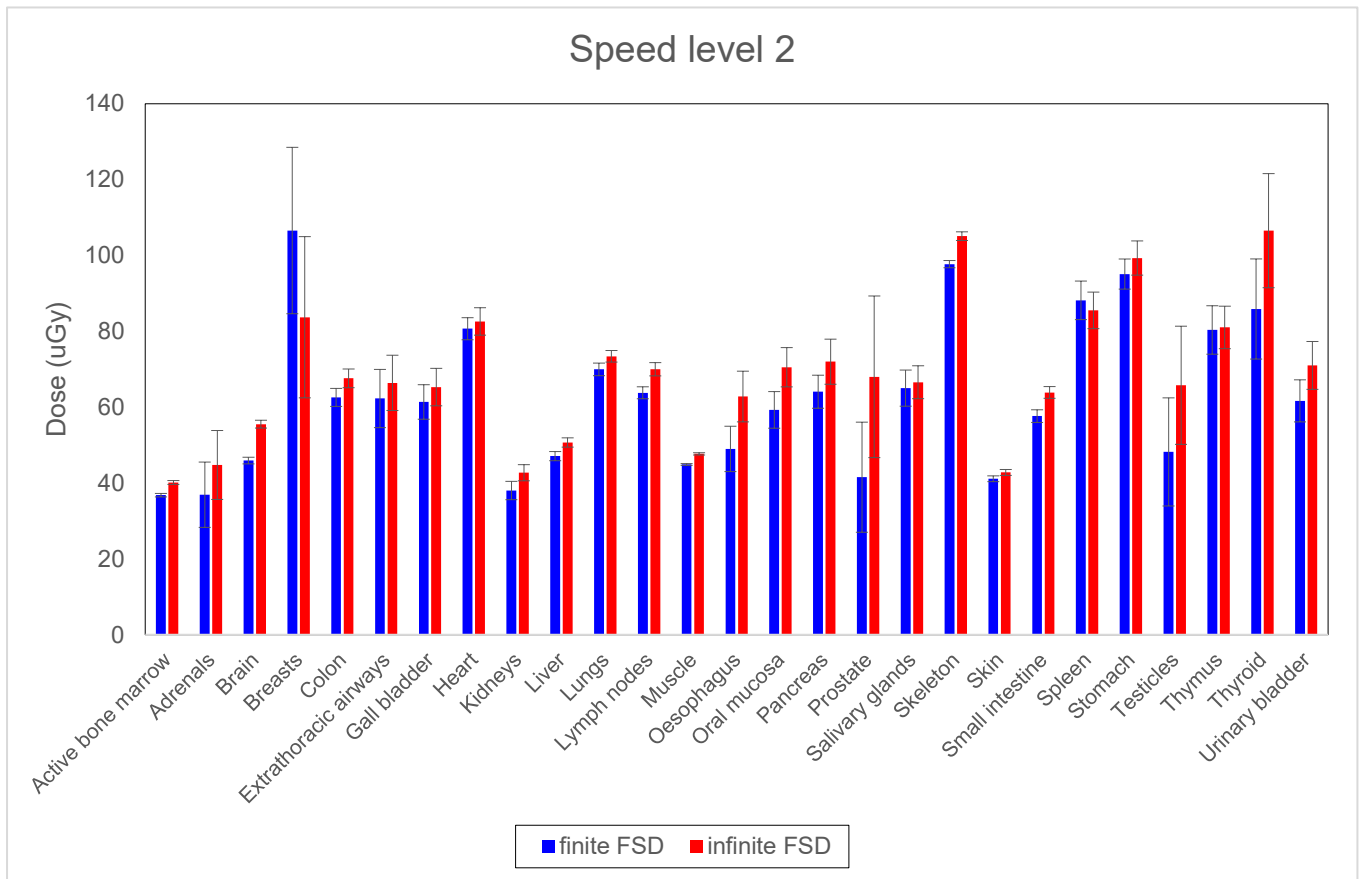


Figure 19 Comparison of EOS organ doses obtained with finite (blue) and infinite (red) FSD. Results refer to EOS acquisitions performed at speed level 2. Error bars represent ± 2 standard deviations.

Figure 21 compares the results obtained at different speed levels for an infinite FSD. In blue, red, and green doses computed for speed levels 2, 3, and 4 are shown, respectively. Organ doses obtained with the fast protocol are 33% and 50% lower than doses obtained at speed levels 3 and 4, respectively. These systematic reductions, which are equal to those found for effective doses, reflect the ratio of total DAP in EOS acquisitions at the different speed levels (see Table 2).

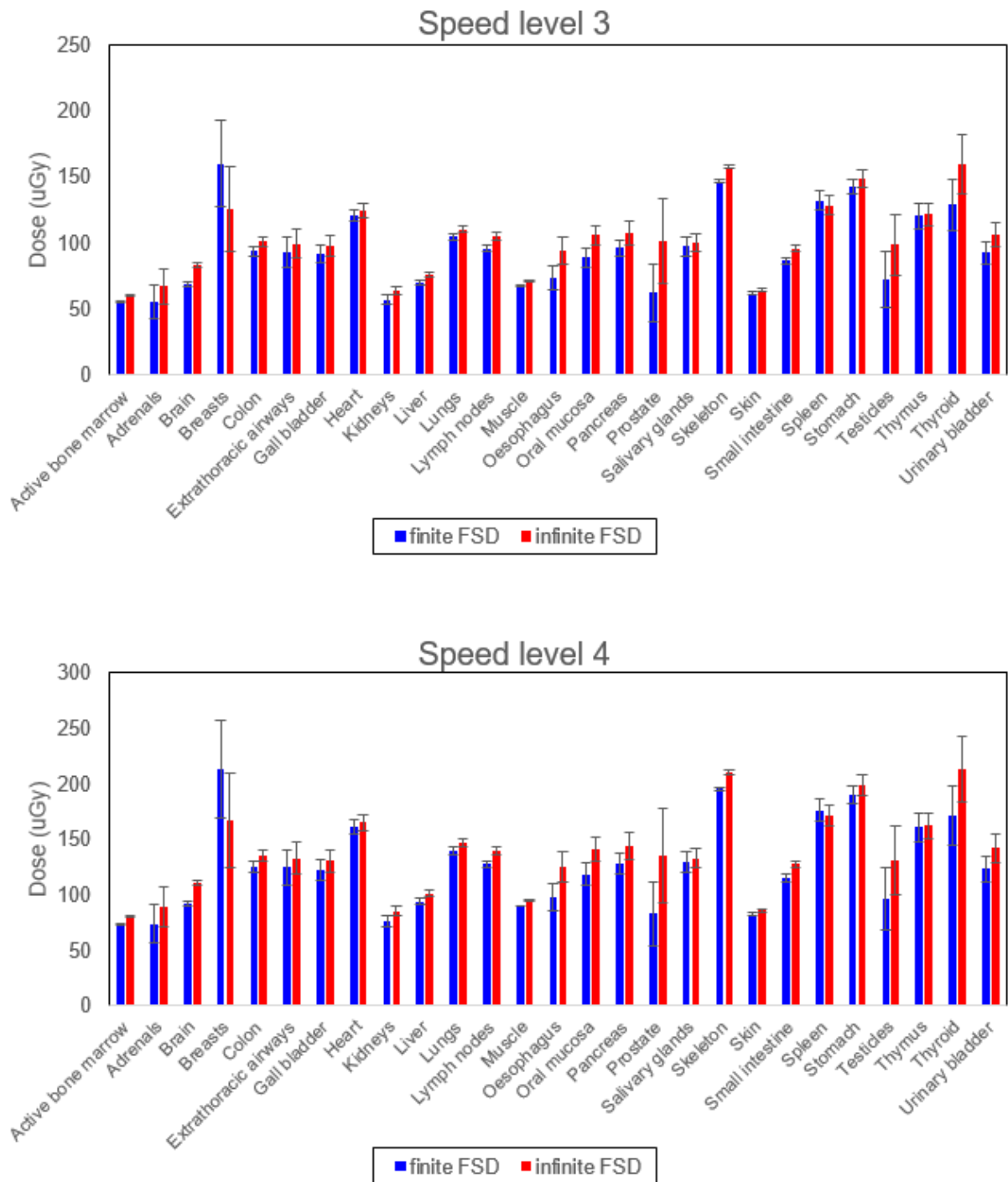


Figure 20 Comparison of organ doses obtained with finite (blue) and infinite (red) FSD for EOS acquisitions performed at speed level 3 (top) and 4 (bottom). Error bars represent ± 2 standard deviations.

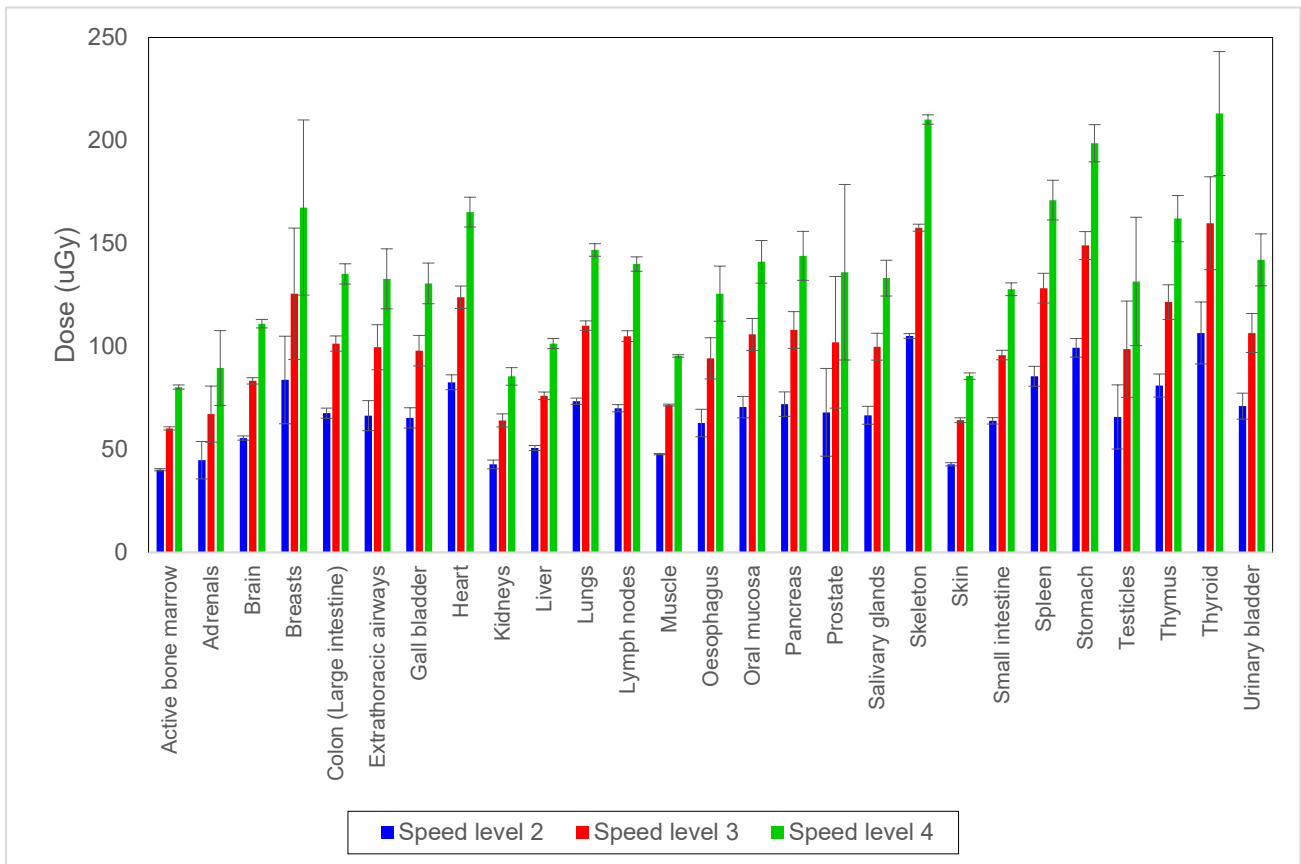


Figure 21 Organ doses computed with *PCXMC 2.0* for EOS acquisitions. In blue, red, and green doses obtained with speed levels 2, 3, and 4 are shown, respectively. Error bars represent ± 2 standard deviations.

Comparison of DR acquisition protocols

Figure 22 compares organ doses obtained for DR acquisitions performed with protocols suited for diagnosis (blue) and follow-up (red). A median dose reduction of 74% was achieved with the low-dose protocol. A higher dose sparing was observed for organs located above the diaphragm (for example breasts, thyroid, thymus, and extrathoracic airways), as the protocol

optimization mainly regards AP and LL projections of the upper body region, as shown in Table 5.

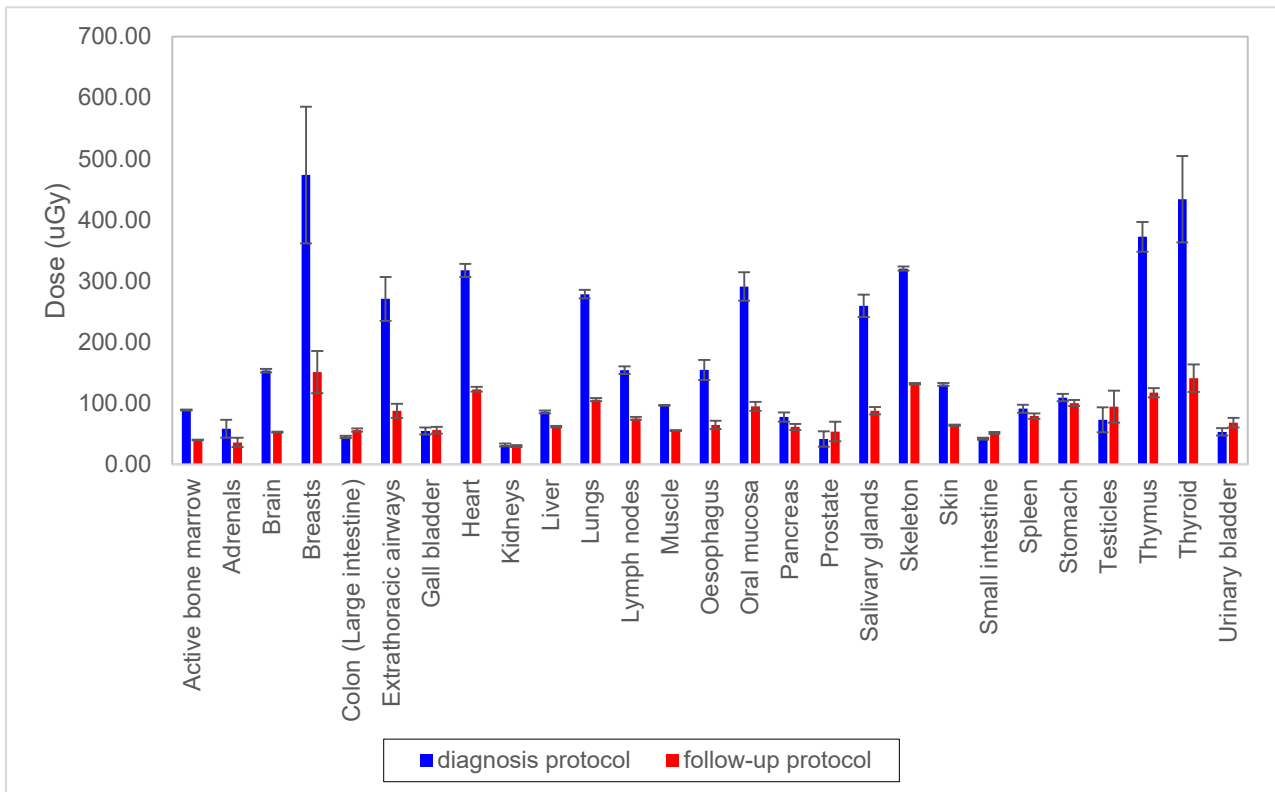


Figure 22 Organ doses obtained with PCXMC 2.0 for DR acquisitions performed with the diagnosis high-dose protocol (blue) and with the follow-up low-dose protocol (red). Error bars represent ± 2 standard deviations.

Simulation of CT examination

The results of *VirtualDose* simulation are shown in Figure 23. Since the software did not provide uncertainties, a relative error of 5% was considered for each dose, as suggested by Ding et al. [45]. Obtained doses ranged from 6.6 mGy (for brain) to 16.6 mGy (for thyroid).

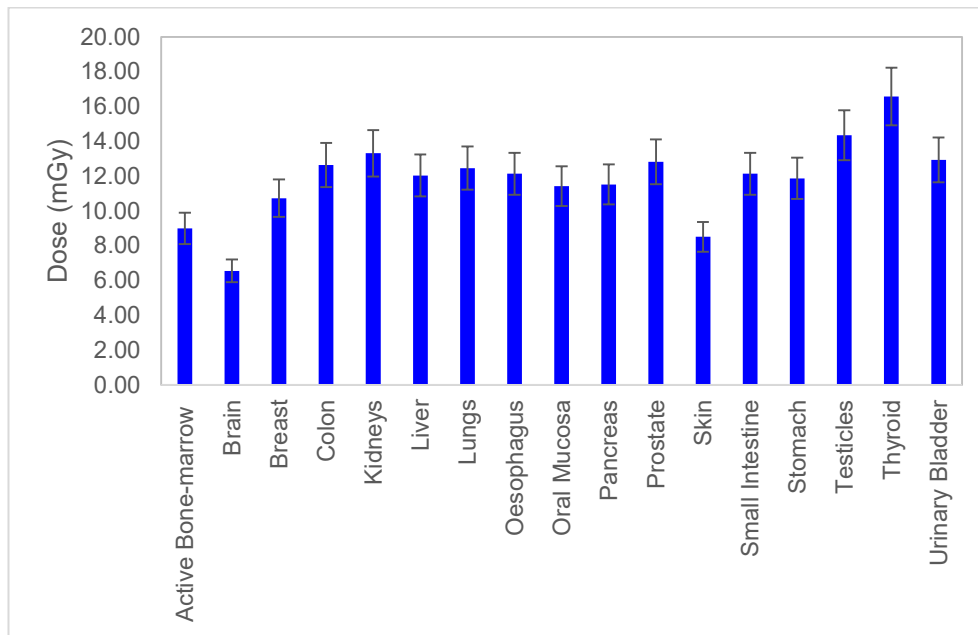


Figure 23 CT organ doses (mGy) calculated with *VirtualDose* software. Error bars represent ± 2 standard deviations.

3.4.b. Dosimetric measurements with TLDs

Preliminary TLD characterization

Repeatability measurements

Values of CV measured for an irradiation dose of 250 μ Gy ranged from 0.6% to 3.2%, with an average value of 1.6%.

Values of CV measured for an irradiation dose of 1.7 mGy ranged from 0% to 3.6%, with an average value of 1.7%.

Linearity evaluation

TLDs responses were corrected for individual sensitivity. Then, for each irradiation dose, the average and standard deviation of the signals were

computed. Figure 24 displays the average values against the irradiation dose. A linear trend was observed up to 28 mGy.

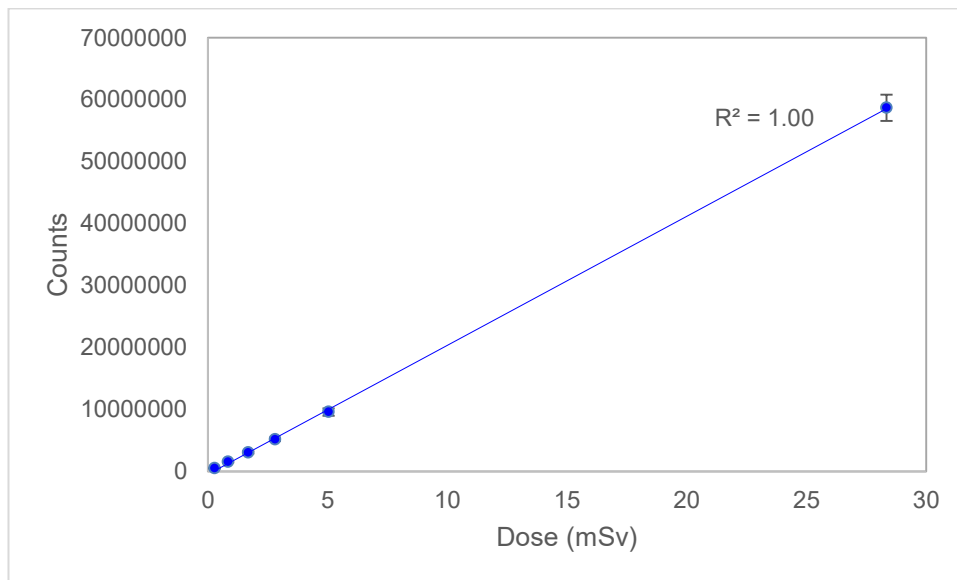


Figure 24 Linearity of TLD response. The irradiation dose is reported on the x-axis. The average TLD signal is reported on the y-axis; error bars represent \pm one standard deviation.

Calibration of TLD dosimeters

Evaluation of energy attenuation

As described in Chapter 2 , the impact of phantom attenuation on the beam quality was evaluated by registering the kVp and HVL values under different thicknesses of PMMA. Two different tube peak potentials were investigated, 80 and 120.

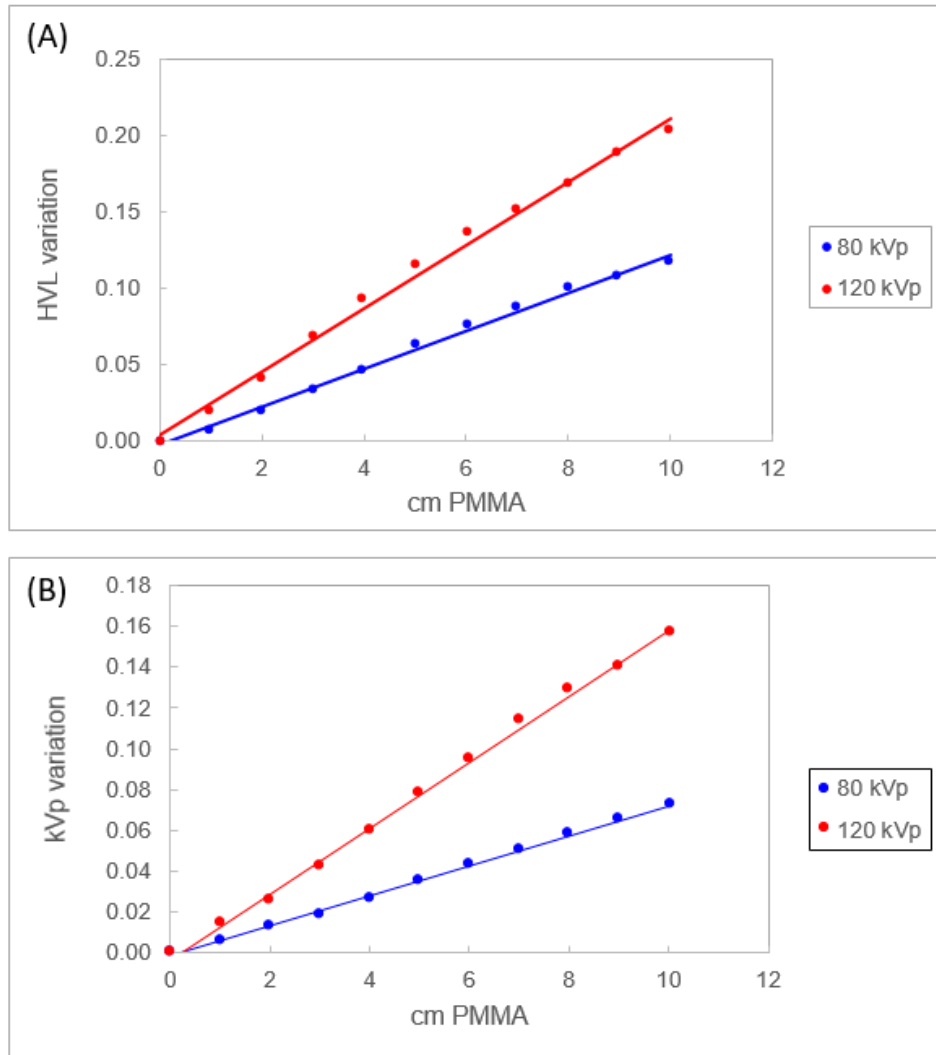


Figure 25 Variation of X-ray beam quality due to in-depth attenuation: (A) HVL: the y-axis represents the HVL variation, normalized to the value measured without attenuation; the x-axis shows the thickness of PMMA. (B) kVp: The y-axis represents the kVp variation, normalized to the value measured without attenuation; the x-axis shows the thickness of PMMA.

Figure 25 shows the obtained results: in (A) the x-axis reports the PMMA thickness, while the y-axis presents the HVL variation. In (B) the kVp variation registered by the multimeter is shown. Differences are expressed as

$$\text{HVL var}_x = \frac{\text{HVL}_0 - \text{HVL}_x}{\text{HVL}_0} \quad \text{and} \quad \text{kVp var}_x = \frac{\text{kVp}_0 - \text{kVp}_x}{\text{kVp}_0},$$

where HVL_x and kVp_x are the values of HVL and kVp measured under x cm of PMMA, and HVL_0 and kVp_0 are the values measured without PMMA. For both quantities a linear relationship was found, which indicates a decrease in the penetrating power of the X-ray beam due to attenuation. Based on this evidence, TLDs were calibrated selecting different source kVp, under the assumption that the kVp measured by the dosimeter roughly represents the quality of the attenuated X-ray beam. A reference thickness of 5 cm PMMA was employed to reproduce the thickness of the 5-year-old dosimetry phantom. Table 13 lists the tube peak potentials selected for TLD calibration.

Calibration energy	Detail
82 kVp	Average value between 83 kVp (EOS AP projection acquisition peak potential) and 81 kVp (value registered under 5 cm PMMA)
102 kVp	Acquisition kVp of EOS LL projection
97 kVp	Value registered under 5 cm PMMA for 102 kVp
66 kVp	Acquisition kVp of DR acquisitions of the upper body. No variation was found under 5 cm PMMA
75 kVp	Acquisition kVp of DR acquisitions of the lower body. No variation was found under 5 cm PMMA
120 kVp	CT acquisition kVp
110 kVp	Value registered under 5 cm of PMMA for 120 kVp

Table 13 Tube peak potentials selected for the calibration of dosimeters. For each value, a brief explanation is proposed.

Calibration curves

TLD responses were corrected for individual sensitivity and background radiation. Then, for each irradiation dose, the average value of the three exposed TLDs was computed. Linear fits were performed to generate the calibration equations. The calibration curves are displayed in Figure 26, Figure 27, and Figure 28, and their parameters are reported in Table 14.

Calibration energy	Slope	Intercept
82 kVp	0.000620 ± 0.000021	-26.6 ± 32.9
97 kVp	0.000590 ± 0.000006	6.8 ± 11.8
102 kVp	0.000577 ± 0.000008	12.0 ± 12.6
66 kVp	0.000607 ± 0.000003	-3.1 ± 4.3
75 kVp	0.000581 ± 0.000013	-10.1 ± 23.2
110 kVp	0.000629 ± 0.000003	-82.4 ± 77.0
120 kVp	0.000605 ± 0.000002	-6.9 ± 50.7

Table 14 Parameters of the calibration curves. Errors represent one standard deviation.

In Figure 26 curves at 82 kVp, 102 kVp, and 97 kVp, which were investigated for calibration in EOS, are displayed. Similarly, Figure 27 presents the curves for DR (66 kVp and 75 kVp) and Figure 28 the curves at 110 kVp and 120 kVp, which were evaluated for CT. For EOS and DR, 95% confidence intervals were superimposed, and no significant difference was observed. For CT, instead, a 3% systematic difference in doses calculated with different calibration curves was found. Based on these results, the following approach was taken to select the calibration curves for organ dose calculation:

1. With reference to Table 13, to take into account the variation of beam quality inside the phantom, the curves for tube peak potentials measured under 5 cm PMMA were selected;
2. The acquisition setup described in Section 2.3.c. was reproduced for each imaging technique.

Thus, for the EOS system, the curves calculated at 82 kVp and 97 kVp were applied to compute the contributions from AP and LL projections, respectively. For DR, curves calculated at 75 kVp and 66 kVp were applied to dosimeters placed in the upper and lower body regions, respectively. For CT, the curve obtained at 110 kVp was applied.

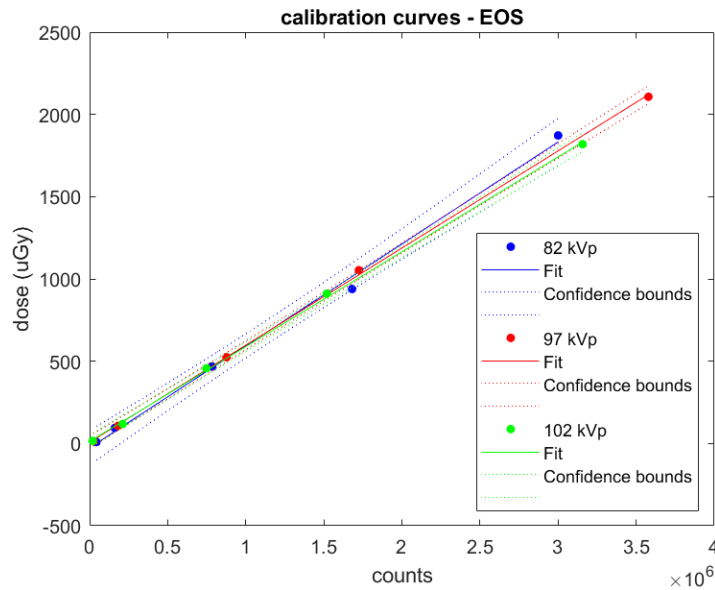


Figure 26 TLDs calibration curves for EOS imaging system. Curves acquired at 82 kVp (blue), 97 kVp (red), and 102 kVp (green) are shown. For each curve, dashed lines represent the 95% confidence interval.

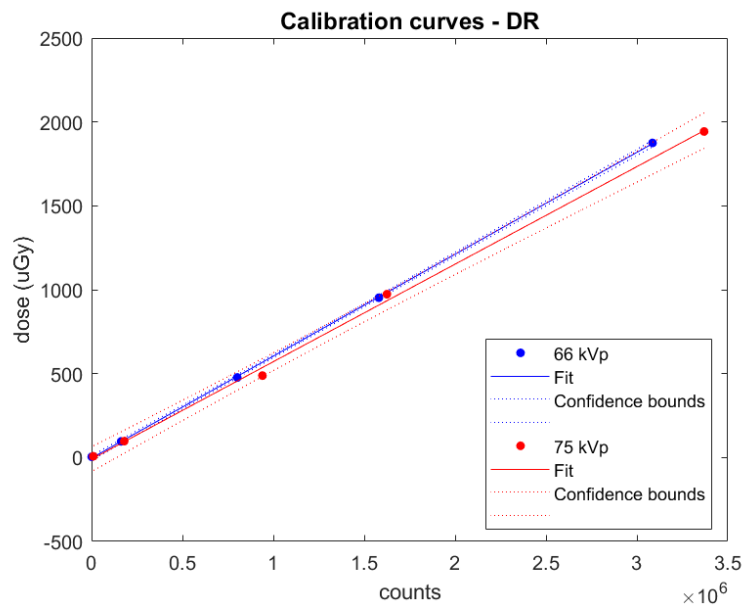


Figure 27 Calibration curves for conventional radiography. Curves acquired at 66 kVp (red) and 75 kVp (blue) are shown. For each curve, dashed lines represent the 95% confidence interval.

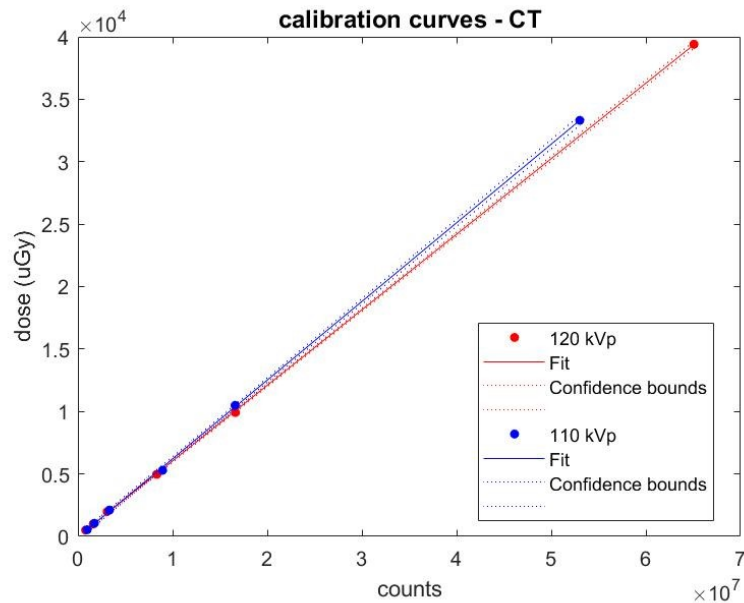


Figure 28 Calibration curves for computed tomography. Curves at 110 kVp (blue) and 120 kVp (red) are shown. For each curve, dashed lines represent the 95% confidence interval.

Organ dose measurements and comparison with simulations

Figure 29 compares organ doses measured in EOS acquisitions performed at speed levels 2 (blue), 3 (red), and 4 (green), respectively.

A similar behavior was noticed for each organ: median increases of 33% and 51% were observed with speed levels 3 and 4 with respect to the fast protocol. As previously mentioned, these values reflect the differences in total DAP registered at the different acquisition speeds.

For EOS acquisitions performed with the fast protocol, experimental measurements are compared with the results of MC simulations in Figure 30. A similar behavior was observed at the other speed levels. Doses measured with TLDs were higher than the simulated for almost all organs, with the exception of pancreas, prostate, and urinary bladder. The observed differences were not statistically significant for 6 out of 17 organs (35%).

On average, *PCXMC* underestimated doses of 20% at speed levels 2 and of 22% at speed levels 3 and 4.

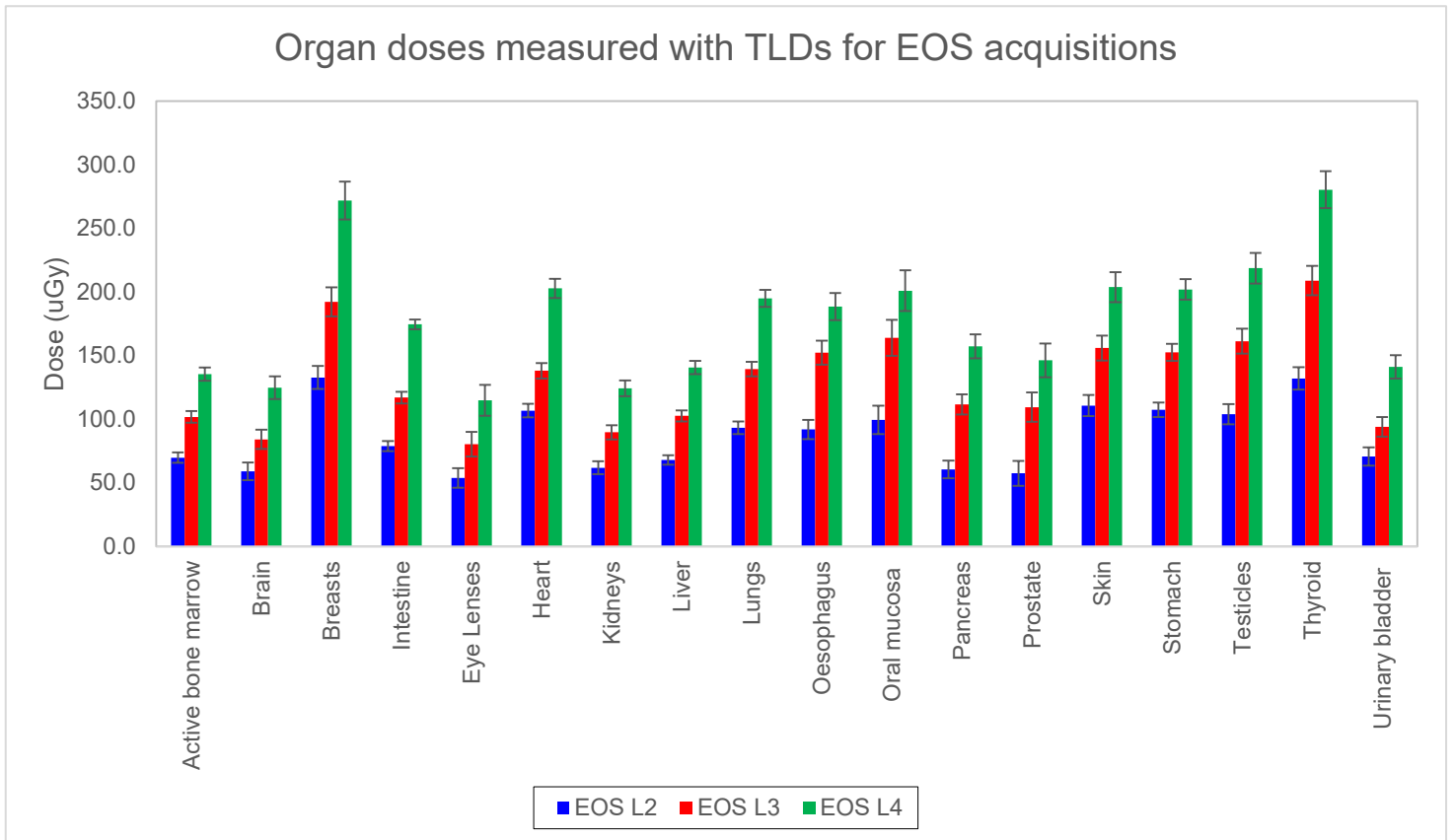


Figure 29 Comparison of organ doses measured with TLDs for EOS acquisitions at speed levels 2 (blue), 3 (red), and 4 (green). Error bars represent ± 2 standard deviations.

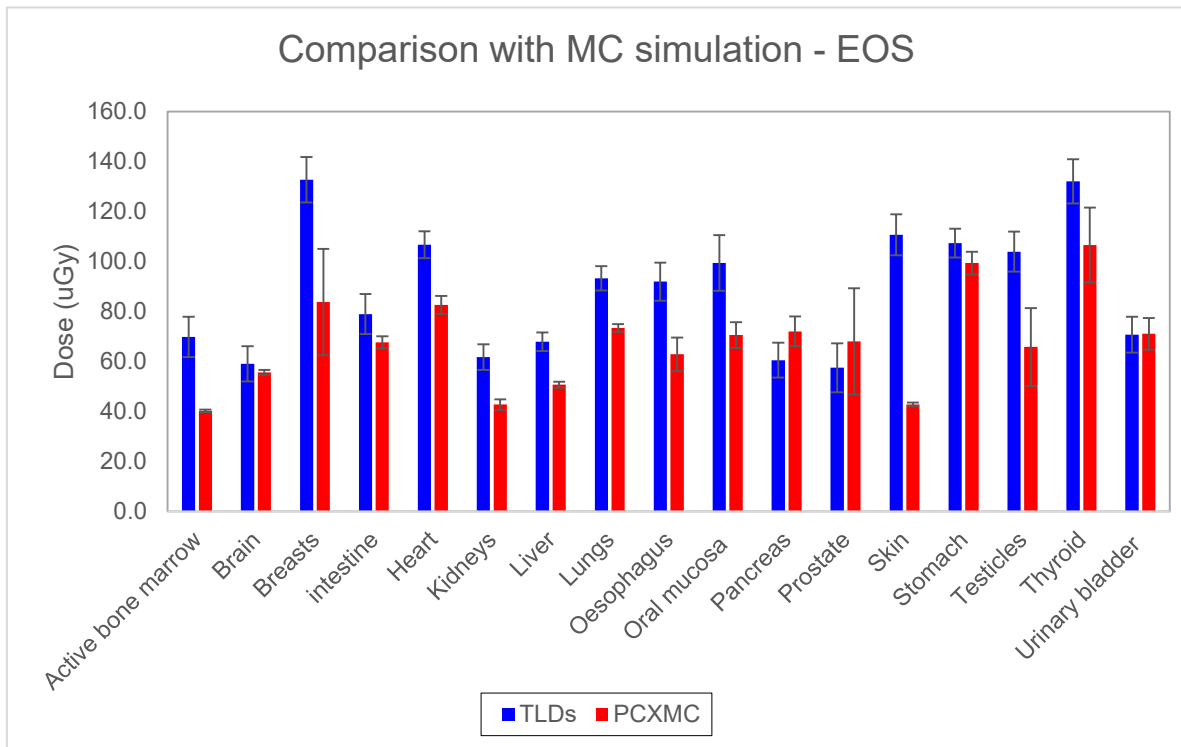


Figure 30 Comparison of organ doses measured with TLDs (blue) and computed with *PCXMC* software (red) for EOS acquisitions performed with the fast protocol. Error bars represent ± 2 standard deviations.

A similar graph is proposed in Figure 32 for DR examinations performed with the acquisition protocol optimized for follow-up. A good agreement was observed between simulated and measured doses. For 12 out of 17 tissues (71%) differences were not statistically significant. The largest variations were registered for urinary bladder (measured dose 64% lower than the simulated), brain (measured dose 49% lower than the simulated) and stomach (measured dose 33% lower than the simulated).

Finally, CT doses are compared in Figure 31. Since *VirtualDose* computes dose to eye lenses, also this organ is considered in the comparison.

As for digital radiography, a good agreement was observed between MC simulation and experimental measurements. *VirtualDose* overestimated doses for almost all organs except for brain and skin; however, taking into

account the uncertainties, only for breasts, oesophagus, oral mucosa, thyroid and urinary bladder differences were statistically significant.

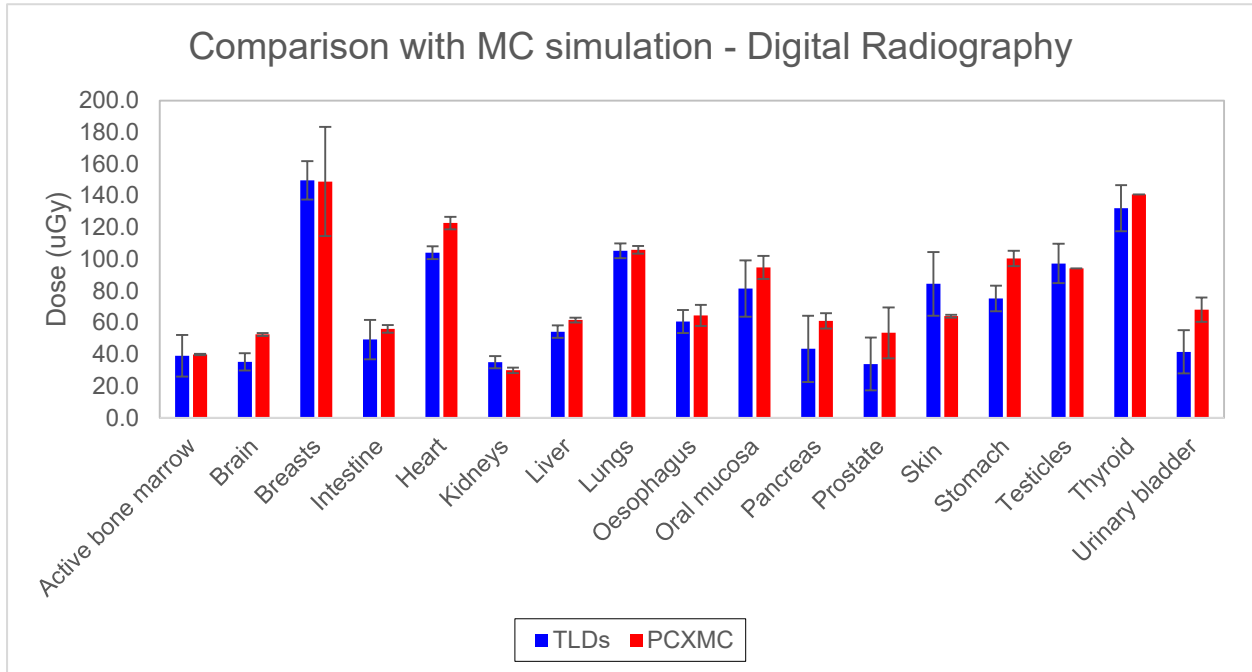


Figure 32 Comparison of organ doses measured with TLDs (blue) and computed with *PCXMC* software (red) for DR acquisitions performed with the low-dose protocol optimized for follow-up. Error bars represent ± 2 standard deviations.

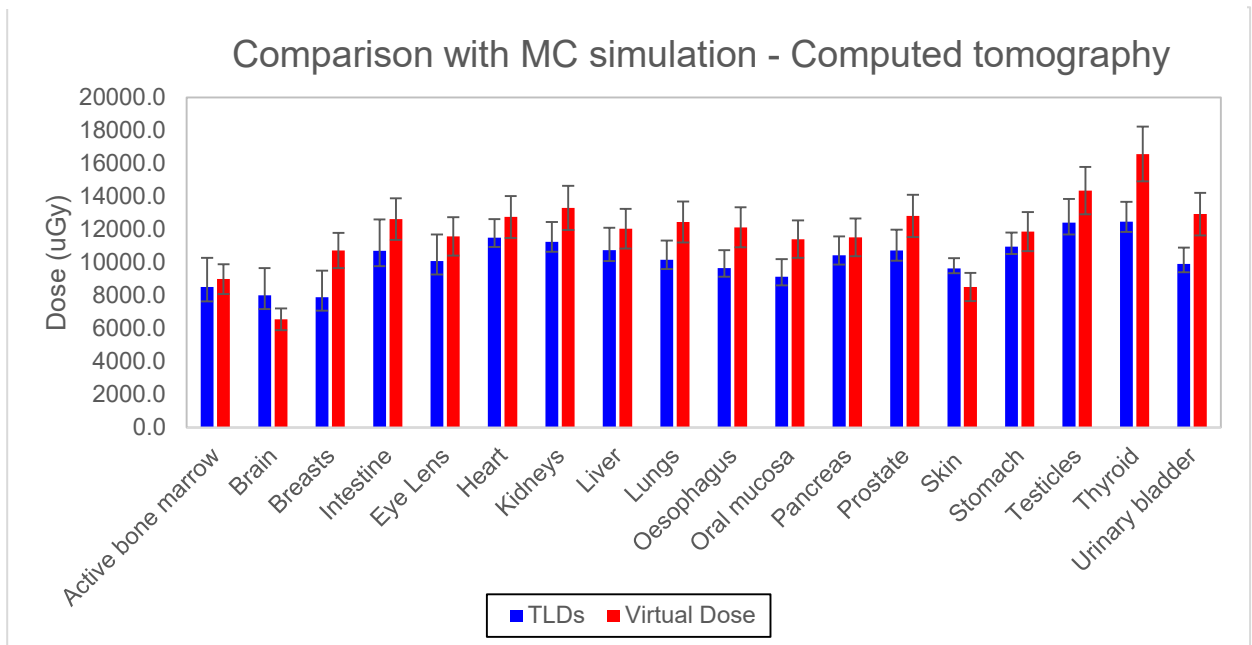


Figure 31 Comparison of organ doses measured with TLDs (blue) and computed with *VirtualDose* software for CT acquisitions. Error bars represent ± 2 standard deviations.

To help the visualization of the outlined results, relative percentage differences between measured and simulated doses, computed as

$$\text{diff \%} = \frac{D_{\text{TLD}} - D_{\text{sim}}}{D_{\text{TLD}}}$$

are shown for each organ and for each imaging technique in Figure 33.

As already described, *PCXMC* underestimated doses for almost all organs in EOS acquisitions. A median difference of -13% was obtained instead for DR acquisitions. The large difference registered for the prostate was not statistically significant, due to the large uncertainty of the simulated dose.

Interestingly, the dose to bladder was considerably underestimated for both DR and CT acquisitions. Since the organ is very small in a 5-year-old child, and its position in the phantom is not easy to be defined, the observed variations could be due to an erroneous position of the dosimeters.

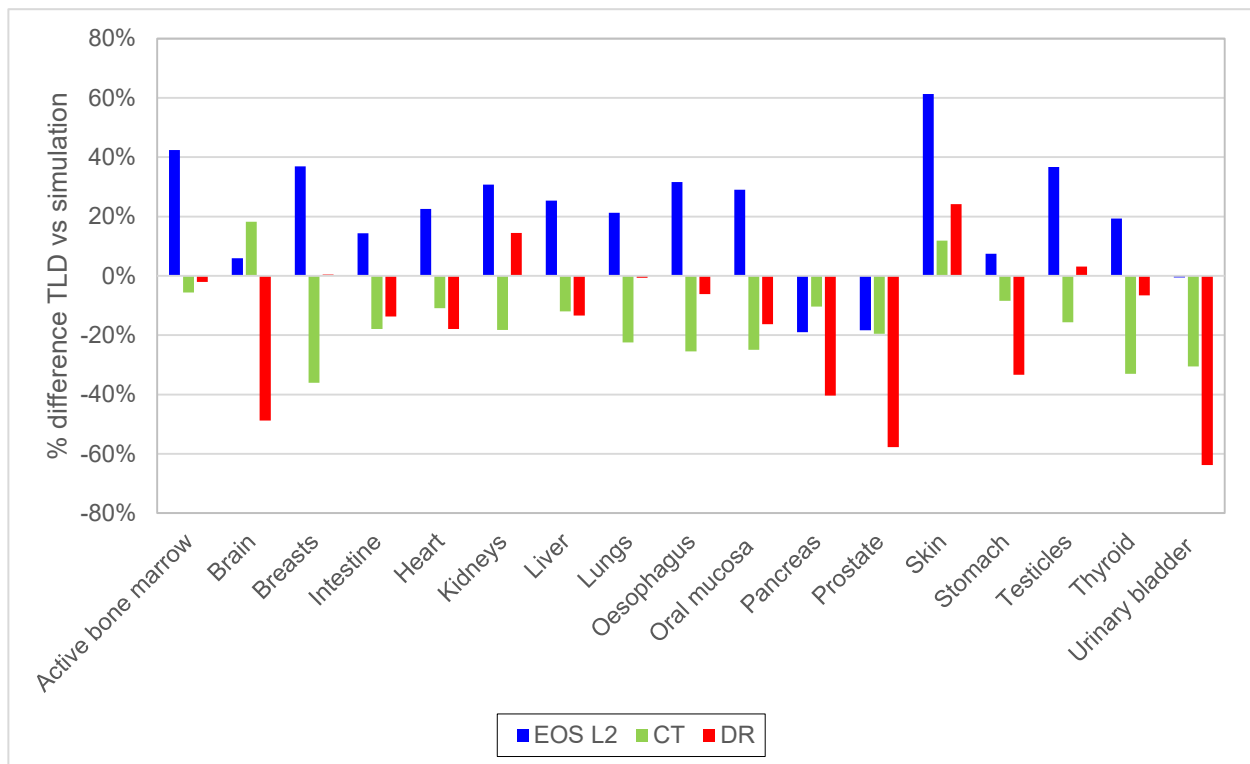


Figure 33 Relative percentage differences between dose measured with TLDs and that computed with MC simulations. Blue, green and red columns refer to EOS (speed level 2), CT, and DR, respectively.

3.4.c. Comparison of imaging techniques

As outlined in the previous Sections, patients with Ollier disease undergo radiological examinations for both diagnosis and follow-up. While diagnosis requires high image quality, instead during follow-up dose reduction should be the leading factor.

This thesis investigates EOS at three speed levels, with different delivered doses, and DR with two acquisition protocols, suited for diagnosis and follow-up, respectively.

Based on the results outlined in the previous paragraphs, *PCXMC* software was considered a reliable tool to compute doses in conventional radiography. For this reason, also doses calculated for the DR diagnostic protocol were considered in the comparison, even if experimental measurements were not performed. The software was instead not suited to simulate EOS acquisitions. Then, for comparison with the other techniques, doses derived by experimental measurements were considered for EOS.

Figure 34 compares organ doses of DR examinations performed with the diagnosis protocol (blue) with doses of EOS acquisitions at speed levels 2 (red), 3 (green), and 4 (purple). DR doses were calculated with MC simulations, while those of EOS were measured with dosimeters. Doses of DR examination were on average higher than EOS doses obtained with the fast protocol, with a median relative difference of 21%. The largest differences were observed for breasts and thyroid, for which DR doses were 72% and 70% higher than the corresponding doses in EOS-fast protocol. EOS doses obtained with the slower protocol were instead higher than DR doses for almost all organs, with the exception of brain, breasts, lungs, oral mucosa, and thyroid.

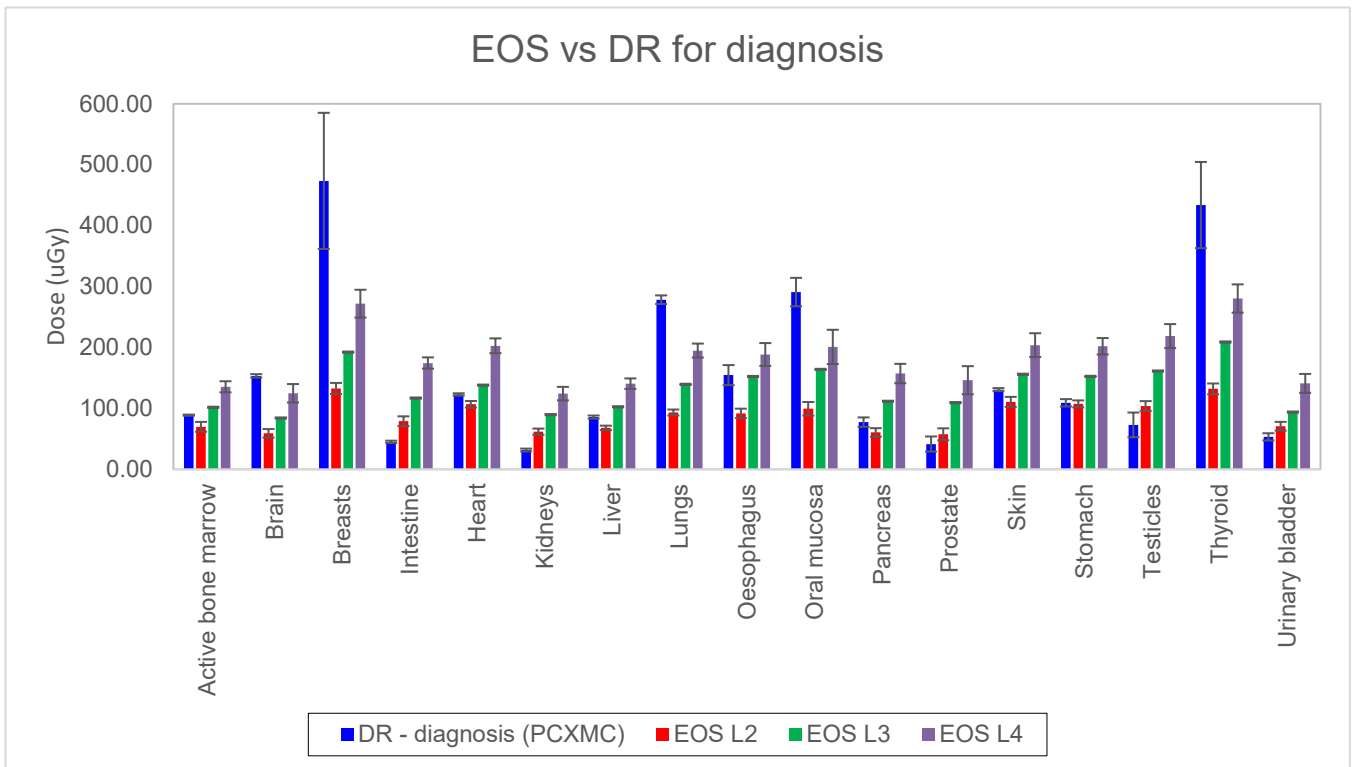


Figure 34 Comparison of organ doses of DR acquisitions performed with the diagnosis protocol (blue), and of EOS examinations at speed levels 2 (red), 3 (green), and 4 (purple). DR doses were computed with MC simulations; EOS doses were instead derived from experimental measurements with TLDs. In both cases error bars represent two standard deviations.

A symmetric graph, in Figure 35, compares EOS doses with those obtained from DR acquisitions performed with the follow-up protocol: here, DR doses were lower than those of EOS for almost all organs, regardless of the speed level. A median reduction of 32% was achieved with DR with respect to EOS fast protocol, with comparable doses to breasts, lungs, thyroid, and oral mucosa.

CT doses were considerably higher than DR and EOS doses. As CT is barely applied for follow-up purposes, only the diagnostic protocol in DR and the slow protocol in EOS were considered for comparison. On average, CT doses were 113 times and 60 times larger than DR and EOS doses, respectively.

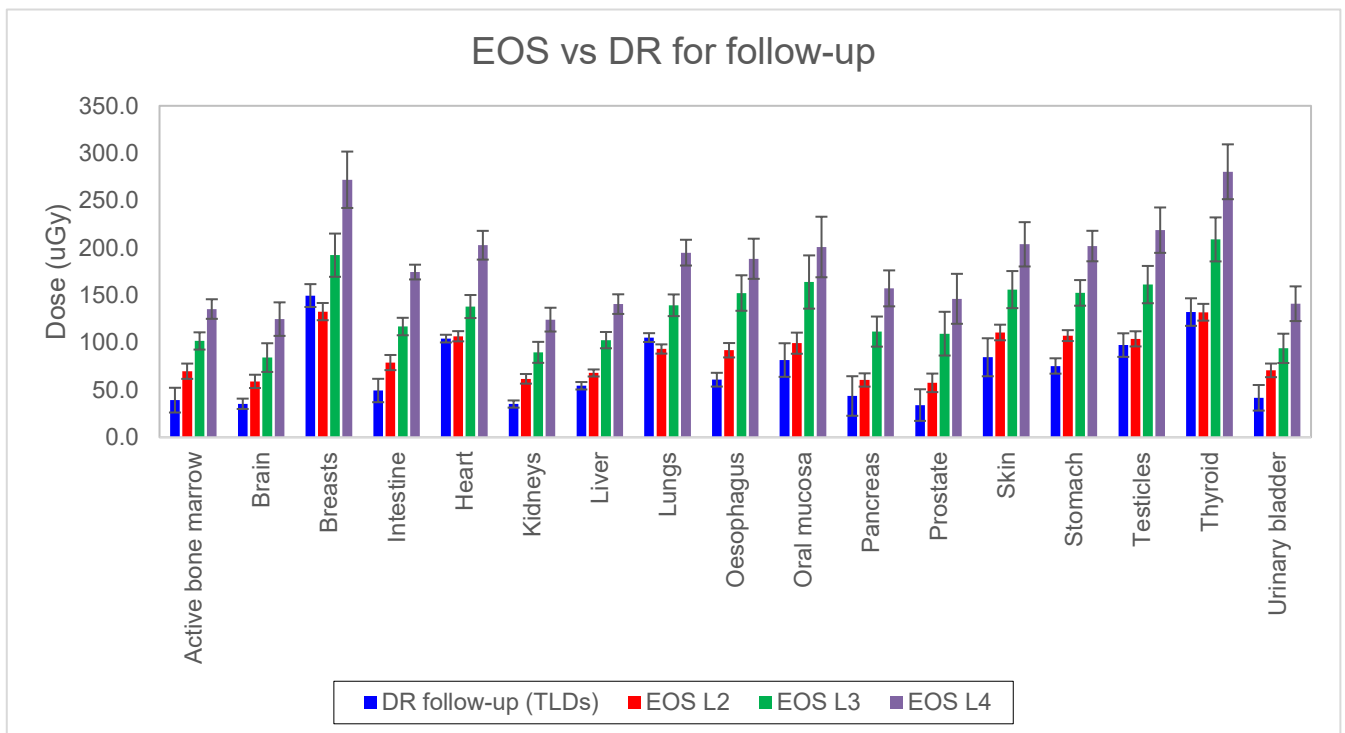


Figure 35 Comparison of organ doses of DR acquisitions performed with the follow-up protocol (blue), and of EOS examinations at speed levels 2 (red), 3 (green), and 4 (purple). For each technique doses were derived from measurements with TLDs. In both cases error bars represent two standard deviations.

3.4.d. Effective dose and risk assessments

Table 15 reports the effective doses computed for each imaging technique with both experimental measurements and MC simulations. *PCXMC* underestimated the EOS effective dose of 24% at speed level 2, and of 26% at speed levels 3 and 4. An excellent agreement was found for DR (1% relative difference). *VirtualDose* overestimated the effective dose of 18%, but the two values were consistent among each other within two standard deviations.

To help the visualization, effective doses are compared in Figure 36. For DR examination performed with the follow-up protocol, the dose calculated with MC simulation is considered; for the other techniques, the value derived from TLD measurements is instead displayed.

	TLDs	MC simulations
	Eff dose (μSv)	Eff dose (μSv)
EOS L2	93.8 \pm 3.6	70.6 \pm 2.8
EOS L3	139.7 \pm 4.4	105.9 \pm 4.2
EOS L4	191.3 \pm 5.3	141.2 \pm 5.6
DR follow-up	79.3 \pm 8.2	79.8 \pm 3.8
DR diagnosis		143.4 \pm 3.5
CT	10008 \pm 679	11847 \pm 1185

Table 15 Effective dose (μSv) derived from measurements with TLDs and provided by MC simulations for each imaging technique and acquisition protocol. Errors represent ± 2 standard deviations.

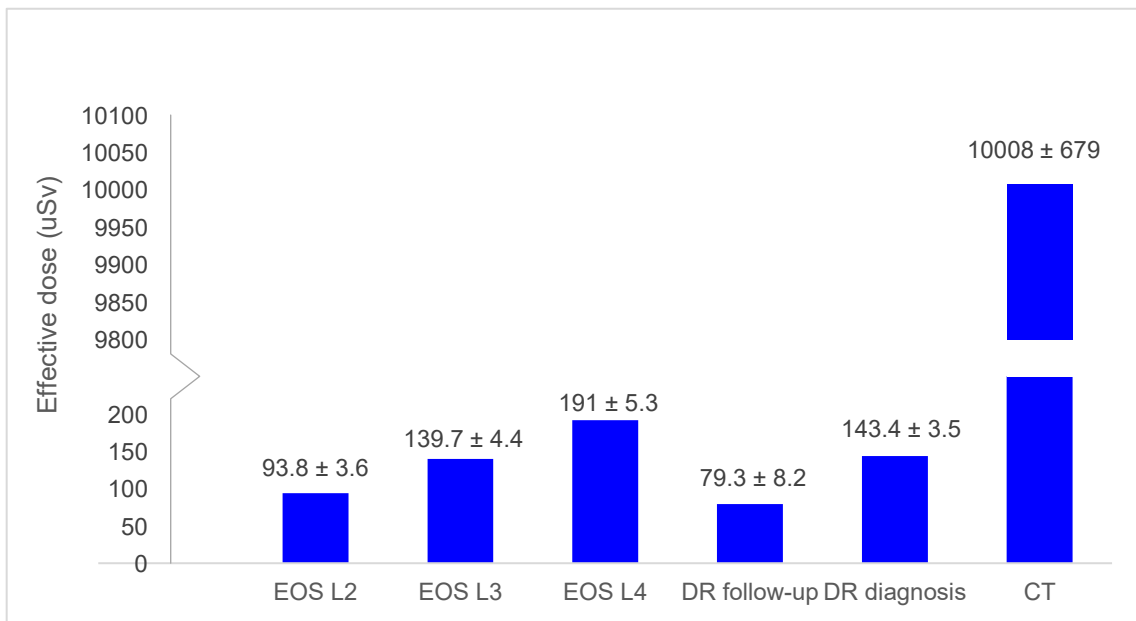


Figure 36 Comparison of effective doses. For DR examination performed with the diagnosis protocol, dose estimated with MC simulation is considered. For the other techniques, doses derived from TLD measurements are selected. The label above each column shows the registered value ± 2 standard deviations.

As for organ doses, the effective dose estimated at speed level 2 was 33% and 50% lower than those at speed levels 3 and 4, respectively. When considering the diagnostic protocol, effective dose in digital radiography examinations was found to be equivalent to that of EOS acquisition performed at speed level 3. The fast protocol in EOS provided a relative dose

reduction of 35%. When considering the follow-up protocol, instead, DR dose was slightly lower than that of EOS acquisition performed at speed level 2, and considerably lower than doses achieved at the other speeds.

The CT dose was much higher than that of the other techniques. Also considering the “high-dose” protocols, CT dose was 52 times the EOS dose and 70 times the DR dose.

Table 16 summarizes the Lifetime Attributable Risk (LAR) of cancer incidence (percentage values) due to a single uniform whole-body examination obtained with different methods for each imaging technique and acquisition protocol. For estimates derived from BEIR VII and Wall et al. nominal risk coefficients, different values are proposed for males and females. A single value is reported for ICRP 103, since a sex and age-averaged coefficient is provided in the report.

	LAR % of cancer incidence				
	BEIR VII		Wall et al (2011)		ICRP 103
	Male	Female	Male	Female	-
EOS L2	0.0017	0.0032	0.0009	0.0013	0.0005
EOS L3	0.0025	0.0047	0.0014	0.0020	0.0008
EOS L4	0.0034	0.0065	0.0019	0.0027	0.0011
DR follow-up	0.0014	0.0027	0.0008	0.0011	0.0004
DR diagnosis	0.0026	0.0048	0.0014	0.0020	0.0008
CT	0.1801	0.3380	0.1001	0.1401	0.0550

Table 16 Lifetime Attributable Risk (LAR) of cancer incidence (percentage value) for the investigated imaging techniques and acquisition protocols. Risks derived from nominal risk coefficients provided by BEIR VII, Wall et al. (2011), and ICRP 103 are reported.

Risk estimates obtained with the HPA method were on average 45% and 59% lower than those derived from the BEIR VII method for males and females, respectively. When compared with ICRP 103, instead, an average risk increase of 80% and 154% was observed for males and females. As for effective doses, the risk associated with the EOS examination with the fast protocol was lower than that of DR when the diagnostic protocol was applied,

and comparable to it when the follow-up protocol was considered. Considering for instance the BEIR VII coefficients and a male patient, risks of 1.7×10^{-5} , 1.4×10^{-5} (-18%), and 2.6×10^{-5} (+53%) were obtained for EOS at speed level 2, DR for follow-up and DR for diagnosis, respectively. Risks increase to 2.5×10^{-5} (+47%) and 3.4×10^{-5} (+100%) when considering speed levels 3 and 4. Similar risks (2.5×10^{-5} and 2.6×10^{-5} - BEIR VII coefficients) were observed for the EOS slow-protocol and the DR diagnostic protocol. LAR computed for CT was instead two orders of magnitude higher (1.8×10^{-3} - BEIR VII coefficient) than that of the other techniques, also when the high-dose protocols were considered.

Chapter 4 Discussion and conclusions

Optimization of radiological procedures is nowadays the most challenging process in radiation protection and the use of new modern technology to reduce the dose is strongly encouraged by International Organizations, and recommended by the Council Directive 2013/59/Euratom [3] and by its Italian transposition D.Lgs 101/2020 [51]. Under this premise, this work evaluated the applicability of the EOS imaging system for the diagnosis and follow-up of Ollier disease. Patients with enchondromatosis undergo frequent radiological examinations from early childhood and possibly for life, and optimization of the radiological procedures is then crucial to provide an accurate assessment of enchondromas with minimum radiological risk.

Diagnostic performance

To evaluate its diagnostic power, EOS was compared with DR and CT, the current gold standards for the diagnosis of Ollier disease. Enchondromas

were simulated with minced pieces of chicken bone, which were demonstrated to reproduce well the attenuation of pediatric cartilage.

The results of the analysis indicate that the diagnostic performance of the EOS system is similar to that of digital radiography, in both the detection and the size evaluation of enchondromas-like inserts. The same conclusions were drawn by two non-expert observers, who were aware of the number and position of the inserts during the analysis, and by two experienced radiologists, who reviewed the images in random order without any information about the placement of the inserts. The expert observers measured a mean difference between the inserts length assessed with EOS and DR and their true length of 6.1 mm and 6.6 mm, respectively. The size was then underestimated with both imaging techniques; however, this was expected since the bidimensional nature of EOS and DR images prevent the identification of the longest length of the inserts.

Interestingly, no image quality loss was observed changing the speed level in EOS acquisitions. Similar results were found also by other authors: Damet et al. [8] observed no influence of the scanning speed either on resolution or noise level. Moreover, Ilharreborde et al. [34] and Law et al. [46] concluded that also the recently introduced *Microdose* protocol can be used in clinical practice for scoliosis examination without altering the quality of the images and obtaining further dose reduction.

Excellent, and comparable, interobserver reproducibility was found for EOS, DR, and CT, both in terms of number detection and size evaluation, thus demonstrating that the EOS imaging system is both accurate and reproducible. Radiologists were able to identify the correct number of inserts in almost all phantom configurations. Only in one case two close inserts were erroneously counted as a single one, in both DR and EOS images.

Excellent intermodality reliability was observed between EOS, DR, and CT and average differences in insert lengths measured with different techniques were lower than the pixel size of the EOS imaging system. This is particularly important to properly evaluate a new diagnostic test, currently not used in the clinical routine [26].

Optimization of digital radiography acquisition protocol

In the first part of the work, only the diagnostic performance of imaging techniques was considered. However, as widely mentioned, patients with Ollier disease often experience long follow-up, with annual examinations possibly for the entire lifetime. The possibility to modify the speed level and the *Microdose* protocol [33] can be fully exploited for follow-up purposes with EOS imaging technique. Doubling the speed velocity provides a DAP reduction of 50%, and different works [10,19] demonstrated that further decrease can be achieved with the *Microdose* protocol. In digital radiography, the level of image quality and delivered dose can be modified, among the other parameters, through the manufacturer-dependent exposure index (EI) [40]. Before investigating the dosimetric performances of the imaging techniques, the DR acquisition protocol was optimized for follow-up purposes, reducing the total DAP from 548.9 mGy cm² to 280 mGy cm², which was comparable to DAP of EOS acquisitions performed with the fast protocol (259 mGy cm²). For the purpose of this study, the variation of image quality was investigated through SdNR evaluations on the bone structures of the anthropomorphic phantom. As expected, a slight decrease in SdNR (relative median and average differences of 1% and 4% respectively) was measured for the follow-up acquisition protocol. However, at least for non-expert observers, no appreciable variation in the visibility of bone structures was noticed.

Dosimetric performance

Dosimetric assessments were performed for each imaging technique with both MC simulations and experimental in-phantom measurements with TLDs. It was decided to use independent methods for dose evaluations to provide reliable results for the EOS system, because no MC software was validated for this device. Luo et al [17], Hui et al. [19], Law et al. [16,46], and Abdenebbi et al. [52] evaluated EOS doses with *PCXMC* software but results were not verified with separate methods. Furthermore, different approaches were taken by the authors to simulate the EOS slot-scanning acquisitions. Law et al divided the scan range in contiguous 0.5 mm-high slot beams and performed different simulations across the whole spine, while Hui et al. performed only one simulation, selecting field dimensions to include the full body. No detailed information about the performed simulation was instead supplied in the other mentioned works. The procedure of Hui et al was applied in this work since it was thought to better reproduce the single-shot irradiation of EOS acquisition.

For completeness, experimental measurements with TLDs were performed also for CT and DR with the follow-up protocol, although *VirtualDose* and *PCXMC* have been demonstrated to well reproduce the examinations [45,47–49].

It is worth noting that the measurement of a point dose, as that performed with TLDs, may not be an accurate measure of the absorbed dose averaged across the entire organ, especially for distributed organs such as active bone marrow and skin. For this reason, as far as possible, we tried to use multiple TLDs for large organs, in order to have a better approximation of the average dose. Furthermore, to take into account the variation in the patient position in repeated exams and the fluctuation of acquisition parameters, for each

imaging technique measurements were repeated three times. The results were then averaged to compute the organ doses. To reduce the uncertainties in the experimental measurements, dosimeters were preliminary characterized in terms of repeatability and linearity. Linearity up to 28 Gy was observed, demonstrating that TLDs were suitable for dose estimations in CT, where high doses were expected. Moreover, a good repeatability in TLD responses (average 1.6%, range from 0.6% to 3.2%) was measured for irradiation doses of 250 μ Sv and 1.7 mSv. As the reproducibility of the dosimeters response could not be tested at the low doses expected in EOS and DR acquisitions, in order to accumulate a sufficient dose we chose to repeat EOS and DR irradiations three times and to normalize the results to a single examination. Dosimeters were calibrated in air. A similar approach was taken by Feng et al. [21] and Hurwitz et al. [53] for dosimetric measurements with TLDs in CT, and by Branchini et al. [9] for measurements in EOS and DR. Different calibration tube peak potentials were investigated to take into account the variation of beam quality inside the phantom. Although not large variations were observed with kVp, distinct calibration curves were applied for each imaging technique to better reproduce the acquisition conditions.

The results of experimental measurements confirmed the reliability of simulation software for evaluation of doses in DR and CT. In both cases differences were not statistically significant for most organs. Moreover, dose to the urinary bladder measured with TLDs was considerably lower than the simulated for both techniques. This could be due to an erroneous placement of the dosimeter inside the phantom, because of difficulties in defining the bladder position in a 5-year-old child. Larger discrepancies were observed instead for the EOS system. *PCXMC* underestimated doses to almost all organs, and differences were statistically significant in 65% of cases for all the speed levels. These results are not surprising, as the software was not

developed to reproduce a scanning device. To better approximate the beam geometry and reduce the effect of beam divergence, an infinite focus-to-skin distance was set in the simulation. This choice effectively produced a median increase of 7% in the computed doses but was not sufficient to match the experimental results. Median relative underestimations of 22% (speed level 2) and 24% (speed levels 3 and 4) were obtained with *PCXMC* with respect to TLD measurements, with largest variations for skin and active bone marrow (67% and 42%). For this reason, doses measured with TLDs were considered the reference for EOS.

Results were compared with those of Damet et al. [8], who performed similar TLD measurements with a pediatric phantom, for an EOS examination of total DAP 570 mGy cm². Good agreement was observed with doses obtained in this study at speed level 4, characterized by comparable DAP (517 mGy cm²). A very good agreement was achieved also with the results of the recent work of Pedersen et al. [10], who performed TLD in-phantom measurements at speed level 4. Relative differences in organ doses registered in the two studies ranged from -11% to 25%, with average and median values of 3% and 1%, respectively. Branchini et al. [9] measured considerably higher doses for all the investigated organs; however, results were not comparable as their measurements were performed at speed level 7 with an adult phantom. Hamzian et al. [18] performed a MC simulation with *PCXMC* for a whole-body examination at speed level 4 and found considerably lower doses than those measured with TLDs in this study. However, a good agreement was observed with the results of our MC simulation (median relative difference of 1%, with large discrepancies only for liver (75%) and bladder (67%)).

EOS fast protocol provided a slight reduction in doses with respect to the DR diagnostic protocol, with the largest sparing for breasts, lungs, oral mucosa,

and thyroid. At speed levels 3 and 4, instead, median increases in organ doses of 17% and 56% were observed with respect to DR. However, DR doses to particularly radiosensitive organs as breasts, lungs, oral mucosa, and thyroid remained considerably higher than those of EOS. Interesting results were obtained with the DR protocol optimized for follow-up. On average, organ doses were halved with respect to the diagnosis protocol, and they were often lower than those obtained with the fast protocol in EOS. With respect to the latter, a median reduction in doses of 35% was observed. Dose to breast, thyroid, lungs, and oral mucosa, which was relatively high for examinations with the diagnostic protocol, in this case were comparable to those obtained with EOS fast protocol.

As expected, CT doses were instead two orders of magnitude larger than those of DR and EOS. No studies could be found in the literature regarding whole-body CT scan examinations in pediatric patients. Feng et al. [21] evaluated delivered doses with TLDs in thorax, abdomen, and pelvis exams. An acceptable agreement was observed with the results obtained in this work: Feng et al registered a dose to breast of 7.9 mGy (thorax examinations) against the 7.8 mSv of this study. Doses to intestine (abdomen) and lungs (thorax) were 6.6 and 5.4 mGy respectively, 40% lower than the 10.5 and 9.3 mGy registered in this work. This was considered acceptable taking into account the variation in acquisition parameters (for instance, the exams in Feng et al work were performed with 110 kV). Unfortunately, $CTDI_{vol}$ was not reported in the article and could not be compared.

Relative uncertainties in doses derived from TLD measurements in EOS, DR, and CT examinations were on average equal to 4%, 9% and 12%, respectively. A similar behavior was observed in the standard deviations of TLDs before dose calculation, where higher fluctuations were observed for CT compared

to the other techniques. These differences are probably related to inaccuracies in the phantom placement in the repeated measurements. Indeed, the positioning of the phantom was easily replicated in the EOS chamber thanks to laser-light guides and to the design of the imaging system. The same was instead more challenging in DR and CT examinations.

Effective dose and risk assessment

Effective doses were computed for each imaging technique, with both MC simulations and TLD measurements following ICRP 103 recommendations. The obtained results reflect the behavior observed for organ doses: *PCXMC* and *VirtualDose* reproduced well the experimental findings in DR and CT acquisitions, while significant underestimations were observed for the EOS system. The effective dose of DR exams performed with the diagnostic protocol (143 μSv) was comparable to that of EOS acquisitions at speed level 3 (140 μSv), and lower than that obtained at speed level 4 (191 μSv). EOS fast protocol provided a considerable dose reduction (to 94 μSv). Extremely similar results were found by Pedersen et al. [10] who measured effective doses of 143 μSv and 196 μSv in pediatric DR and EOS (level 4) examinations, respectively. Good agreement was found also with Damet et al., if we assume the 200 μSv effective dose was registered for an examination performed at speed level 4. When considering the follow-up protocol, effective dose in DR examinations was reduced to 80 μSv , comparable to but lower than that of EOS acquisitions with the fast protocol. Finally, the effective dose in CT examination was 52 times the EOS dose obtained for the slow protocol, and 70 times the DR dose measured with the diagnostic protocol. These ratios increased to 108 and 125 when the low-dose protocols were considered.

Interestingly, extremely lower effective doses were found in the literature for EOS *Microdose* protocol: Pedersen et al. [10] estimated an effective dose of

27 μSv for a whole-body AP-LL examination of a 5-year-old child, while Law et al. [46] founds further lower dose of 7 μSv for the same exam performed in PA-LL orientation. These promising results lead to consider *Microdose* protocol a valid and powerful instrument to reduce the dose especially for follow-up purposes.

Effective doses computed with TLDs were used to estimate LAR of cancer incidence in a whole-body uniform examination performed during childhood. Nominal risk coefficients provided by HPA (Wall et al. [50]), BEIR VII [44] and ICRP 103 [43] were used. While ICRP provides a single coefficient risk, averaged over all ages and both sexes, the other two methods supply age and sex-specific coefficients. The HPA study applied the ICRP risk model and cancer rates of a Euro-American population, while the BEIR VII model relates to the American population. Risk coefficients (and so the LAR) predicted by the BEIR model for the 0-9 year age band are higher than the corresponding of HPA by a factor 1.8 for males, and 2.4 for females, due to differences in the DDREF (dose and dose rate effectiveness factor) of the models and to the different reference populations. As pointed out by Wall et al., these substantial differences serve to highlight the large uncertainties associated with risk estimates. However, LAR is a useful and simple tool to compare different imaging techniques. In this work, risks were calculated also with the ICRP 103 nominal coefficient, averaged over all ages and sexes, and applied to uniform whole-body irradiation. When the ICRP 103 coefficient was considered, the results show a considerable underestimation of the risk with respect to the sex-averaged risks of HPA (range from 52% to 58% for the different imaging techniques), and BEIR VII (range from 78% to 80% for the different imaging techniques). Only a single whole-body examination was considered for LAR estimation. The risk associated with multiple exams in the follow-up period is hard to evaluate since the effective dose calculated for a

pediatric patient is not a good surrogate for dose in adolescence and adulthood. However, assuming annual examinations, a rough estimate of cumulative risk can be performed in the range from 5 to 10 years, in which both BEIR VII and HPA nominal risk coefficients do not change.

By using EOS fast protocol for both diagnosis and follow-up, 5 examinations results in a risk of cancer incidence of 8.5 in 100000 (BEIR VII). Assuming instead to apply the diagnosis and follow-up protocols for the first and the other four DR examinations, respectively, a risk of 8.2 in 100000 (BEIR VII) is estimated.

Limitations of the work

This work has some limitations. First of all, the enchondromas-like inserts were attached on the external surface of the phantom, which is not what happens in enchondromatosis. However, this was the best approximation possible, as lesions could not be placed inside the phantom. Moreover, radiologists did not review the images acquired with the DR follow-up protocol, which showed the best dosimetric performances. Image quality was tested only with SdNR in-phantom evaluations, which could be not sufficient to verify the visibility of cartilaginous structures. Both DR and EOS examinations were performed with AP and LL projections. In general, technologists prefer AP orientation in EOS acquisitions because it is easier to position the patient and to communicate with him. PA orientation, indeed, requires the patient to face the wall, which can produce anxiety and a tendency to fidget especially in children [17]. However, different works [10,17,54] documented that obtaining radiographs in the PA position decreases the amount of absorbed dose in most radiosensitive organs, and thus the effective dose. Finally, only pediatric protocols were considered in the study, although it is known that follow-up might continue during

adulthood. Different results could be achieved with adult patients, especially regarding dose sparing with the EOS imaging system with respect to DR.

Conclusions

To sum up, as claimed in other works [8,9], when applied for diagnostic purposes, EOS provides dose reduction compared to DR. However, the optimization of DR acquisition protocol for follow-up allows to further lower the dose and to improve the EOS dosimetric performance. At this point, it should be noted that most of the studies that investigated the EOS dosimetric performances only considered adult patients. To our knowledge, Pedersen et al. were the first to study its application in pediatric exams, and they observed lower doses in digital radiography. These results are probably attributable to the international effort in the optimization of pediatric conventional imaging protocols. Furthermore, despite the relative novelty of the EOS imaging technique, the device used in this work was installed at IRCCS Istituto Ortopedico Galeazzi in 2013, and it is not as modern as the investigated digital radiography system.

Nonetheless, the study demonstrated that EOS diagnostic performance is similar to those of conventional radiography and CT, the current gold standards in the evaluation of Ollier disease. Furthermore, speed level did not affect the visibility of the inserts on the phantom, and so the fast – low dose – acquisition protocol can be applied without influencing the capability of radiologists to detect and measure enchondromas. These data lead to consider EOS as a potential imaging tool technique for detecting and following Ollier disease over time, ensuring a low radiation exposure. Furthermore, since enchondromas are benign bone lesions, these considerations can be extended to other bone pathologies.

A drawback of EOS is the increased risk of motion artifacts related to the fact that the acquisition is performed with the patient in a standing position and has a duration of a few seconds. This limitation can be partly overcome by selecting the fast acquisition protocol, as it was demonstrated that the visibility of structures is not affected by the speed level. On the other hand, the full length of the body can be imaged with the EOS system with a single acquisition, removing the need for digital stitching or manual joining of multiple images. Furthermore, since the X-ray sources move in synchronous fashion, true-to-size images can be acquired, avoiding the magnification error inherent in digital radiography because of the beam divergence. Finally, the entire duration of the exam, from preparation and positioning of the patient to X-ray exposure, is considerably lower in EOS exams than in other techniques, an important feature especially for pediatric applications.

This work demonstrates that the EOS system has the same diagnostic capability as digital radiography and computed tomography to detect and measure enchondromas-like inserts in a pediatric phantom. Although no considerable dose reduction was found with respect to digital radiography when applied for follow-up purposes, EOS fast protocol still provides low doses, and it may then be considered a valid solution for monitoring patients with multiple enchondromas. In the future, the implementation of the *Microdose* protocol may be envisioned in order to further reduce the dose. Furthermore, these considerations could be potentially extended to other bone pathologies. However, the work considered only in-phantom evaluations, and clinical studies are required to confirm the results.

Index of figures, tables and graphs

The Figures

FIGURE 1 EOS IMAGING SYSTEM.....	17
FIGURE 2 CIRS ATOM DOSIMETRY PHANTOM FAMILY. FROM LEFT TO RIGHT THE ADULT MALE, ADULT WOMEN, PEDIATRIC 10-YEAR-, 5-YEAR-, 1-YEAR-OLD AND NEWBORN MODELS.....	17
FIGURE 3 EXAMPLE OF HOLES POSITION AND ORGAN IDENTIFICATION IN CIRS ATOM DOSIMETRY PHANTOMS. THE SELECTION OF POSITIONS IS SUPPORTED BY ANATOMICAL INFORMATION AND EACH HOLE IS PROVIDED WITH A UNIQUE ID NUMBER.	19
FIGURE 4 EXAMPLE OF CARTILAGE HU EVALUATION. CORONAL AND SAGITTAL VIEWS WERE USED TO LOCATE INTERVERTEBRAL DISCS IN THE AXIAL PROJECTIONS.	20
FIGURE 5 <i>LEFT</i> : PICTURE OF EOS ACQUISITION SETUP. THE PHANTOM WAS PLACED AT THE CENTER OF THE SCANNING CHAMBER AND CENTERED USING LASER-LIGHTS GUIDES. THE PICTURE WAS TAKEN BEFORE THE INSERTS WERE HUNG ON THE PHANTOM. <i>RIGHT</i> : EXAMPLES OF EOS AP AND LL PROJECTION OBTAINED WITH PHANTOM CONFIGURATION A. THE RED ARROWS INDICATE SOME OF THE ENCHONDROMAS.	22
FIGURE 6 EXAMPLES OF CONVENTIONAL RADIOGRAPHS FOR PHANTOM CONFIGURATION A. THE RED ARROWS INDICATE SOME OF THE ENCHONDROMAS. A) AP PROJECTION OF THE UPPER BODY B) AP PROJECTION OF THE LOWER BODY; C) LL PROJECTION OF THE UPPER BODY AND D) LL PROJECTION OF THE LOWER BODY.....	23
FIGURE 7 ACQUISITION OF THE PHANTOM IN COMPUTED TOMOGRAPHY. THE PHANTOM WAS POSITIONED IN THE CENTER OF THE SCANNER USING LASER GUIDES.	24
FIGURE 8 DEFINITION OF THE GEOMETRIC SETUP AND PATIENT CHARACTERISTICS IN <i>PCXMC 2.0</i>	29
FIGURE 9 <i>VIRTUALDOSE</i> PARAMETER SELECTION PANEL WITHIN THE <i>RDIM</i> PLATFORM. PARAMETERS ARE READ FROM THE <i>DICOM</i> FILE. FEATURES NOT AVAILABLE IN THE <i>DICOM</i> OBJECTS (WEIGHT, HEIGHT, ANATOMICAL REGION AND PHANTOM TYPE) CAN BE SELECTED BY THE USER.	32
FIGURE 10 <i>PCXMC 2.0</i> INTERFACE: REPRESENTATION OF AP PROJECTION FIELD IN EOS ACQUISITIONS.	34
FIGURE 11 DEFINITION OF THE SCAN GEOMETRY WITHIN THE <i>VIRTUALDOSE</i> SOFTWARE. THE SCAN RANGE IS DEFINED ON THE TOPOGRAMS AND PROJECTED ON THE SELECTED PHANTOM.....	36

FIGURE 12 AVERAGE HOUNSFIELD UNITS OF CHILDREN CARTILAGE (RED), OLLIER SIMULATED ENCHONDROMAS (ORANGE), CHILDREN BONE (GREEN) AND PHANTOM BONE (BLUE). ERROR BARS REPRESENT \pm ONE STANDARD DEVIATION.....	44
FIGURE 13 INTEROBSERVER REPRODUCIBILITY IN COMPUTED TOMOGRAPHY. THE MEAN OF THE MEASURED LENGTHS IS REPORTED ON THE X-AXIS; THE DIFFERENCE IS REPORTED ON THE Y-AXIS. THE BLUE LINE CORRESPONDS TO THE BIAS. THE RED LINES DEFINE THE LIMITS OF AGREEMENT.	46
FIGURE 14 INTEROBSERVER REPRODUCIBILITY IN EOS ACQUISITIONS AT SPEED LEVEL 2. THE MEAN OF THE MEASURED LENGTHS IS REPORTED ON THE X-AXIS; THE DIFFERENCE IS REPORTED ON THE Y-AXIS. THE BLUE LINE CORRESPONDS TO THE BIAS. THE RED LINES DEFINE THE LIMITS OF AGREEMENT.....	47
FIGURE 15 INTEROBSERVER REPRODUCIBILITY IN CONVENTIONAL RADIOGRAPHY. THE MEAN OF THE MEASURED LENGTHS IS DISPLAYED ON THE X-AXIS; THE DIFFERENCE IS REPORTED ON THE Y-AXIS. THE BLUE LINE CORRESPONDS TO THE BIAS. THE RED LINES DEFINE THE LIMITS OF AGREEMENT.	48
FIGURE 16 INTERMODALITY RELIABILITY OF INSERT LENGTH MEASUREMENTS AMONG (A) EOS AND DR, AND (B) EOS AND CT. THE MEAN OF THE LENGTHS MEASURED FROM DIFFERENT TECHNIQUES IS DISPLAYED ON THE X-AXIS; THE DIFFERENCE IS REPORTED ON THE Y-AXIS. THE BLUE LINE CORRESPONDS TO THE BIAS. THE RED LINES DEFINE THE LIMITS OF AGREEMENT.....	50
FIGURE 17 COMPARISON OF DAP VALUES (MGY CM ²) IN AP AND LL PROJECTIONS OF DR ACQUISITIONS PERFORMED WITH THE DIAGNOSTIC (BLUE) AND FOLLOW-UP (RED) PROTOCOLS.	51
FIGURE 18 POSITION OF THE ROIS FOR SdNR EVALUATION. TWO ROIS WERE CONSIDERED FOR EACH MEASUREMENT, ONE PLACED INSIDE THE BONE STRUCTURE, AND THE OTHER ON AN ADJACENT BACKGROUND REGION.	52
FIGURE 19 COMPARISON OF EOS ORGAN DOSES OBTAINED WITH FINITE (BLUE) AND INFINITE (RED) FSD. RESULTS REFER TO EOS ACQUISITIONS PERFORMED AT SPEED LEVEL 2. ERROR BARS REPRESENT \pm 2 STANDARD DEVIATIONS.	54
FIGURE 20 COMPARISON OF ORGAN DOSES OBTAINED WITH FINITE (BLUE) AND INFINITE (RED) FSD FOR EOS ACQUISITIONS PERFORMED AT SPEED LEVEL 3 (TOP) AND 4 (BOTTOM). ERROR BARS REPRESENT \pm 2 STANDARD DEVIATIONS.	55
FIGURE 21 ORGAN DOSES COMPUTED WITH PCXMC 2.0 FOR EOS ACQUISITIONS. IN BLUE, RED, AND GREEN DOSES OBTAINED WITH SPEED LEVELS 2, 3, AND 4 ARE SHOWN, RESPECTIVELY. ERROR BARS REPRESENT \pm 2 STANDARD DEVIATIONS.....	56
FIGURE 22 ORGAN DOSES OBTAINED WITH PCXMC 2.0 FOR DR ACQUISITIONS PERFORMED WITH THE DIAGNOSIS HIGH-DOSE PROTOCOL (BLUE) AND WITH THE FOLLOW-UP LOW-DOSE PROTOCOL (RED). ERROR BARS REPRESENT \pm 2 STANDARD DEVIATIONS.	57

FIGURE 23 CT ORGAN DOSES (MGY) CALCULATED WITH <i>VIRTUALDOSE</i> SOFTWARE. ERROR BARS REPRESENT ± 2 STANDARD DEVIATIONS.	58
FIGURE 24 LINEARITY OF TLD RESPONSE. THE IRRADIATION DOSE IS REPORTED ON THE X-AXIS. THE AVERAGE TLD SIGNAL IS REPORTED ON THE Y-AXIS; ERROR BARS REPRESENT \pm ONE STANDARD DEVIATION.	59
FIGURE 25 VARIATION OF X-RAY BEAM QUALITY DUE TO IN-DEPTH ATTENUATION: (A) HVL: THE Y-AXIS REPRESENTS THE HVL VARIATION, NORMALIZED TO THE VALUE MEASURED WITHOUT ATTENUATION; THE X-AXIS SHOWS THE THICKNESS OF PMMA. (B) kVP: THE Y-AXIS REPRESENTS THE kVP VARIATION, NORMALIZED TO THE VALUE MEASURED WITHOUT ATTENUATION; THE X-AXIS SHOWS THE THICKNESS OF PMMA.....	60
FIGURE 26 TLDs CALIBRATION CURVES FOR EOS IMAGING SYSTEM. CURVES ACQUIRED AT 82 kVP (BLUE), 97 kVP (RED), AND 102 kVP (GREEN) ARE SHOWN. FOR EACH CURVE, DASHED LINES REPRESENT THE 95% CONFIDENCE INTERVAL.....	63
FIGURE 27 CALIBRATION CURVES FOR CONVENTIONAL RADIOGRAPHY. CURVES ACQUIRED AT 66 kVP (RED) AND 75 kVP (BLUE) ARE SHOWN. FOR EACH CURVE, DASHED LINES REPRESENT THE 95% CONFIDENCE INTERVAL.....	63
FIGURE 28 CALIBRATION CURVES FOR COMPUTED TOMOGRAPHY. CURVES AT 110 kVP (BLUE) AND 120 kVP (RED) ARE SHOWN. FOR EACH CURVE, DASHED LINES REPRESENT THE 95% CONFIDENCE INTERVAL....	64
FIGURE 29 COMPARISON OF ORGAN DOSES MEASURED WITH TLDs FOR EOS ACQUISITIONS AT SPEED LEVELS 2 (BLUE), 3 (RED) AND 4 (GREEN). ERROR BARS REPRESENT ± 2 STANDARD DEVIATIONS.....	65
FIGURE 30 COMPARISON OF ORGAN DOSES MEASURED WITH TLDs (BLUE) AND COMPUTED WITH <i>PCXMC</i> SOFTWARE (RED) FOR EOS ACQUISITIONS PERFORMED WITH THE FAST PROTOCOL. ERROR BARS REPRESENT ± 2 STANDARD DEVIATIONS.	66
FIGURE 32 COMPARISON OF ORGAN DOSES MEASURED WITH TLDs (BLUE) AND COMPUTED WITH <i>VIRTUALDOSE</i> SOFTWARE FOR CT ACQUISITIONS. ERROR BARS REPRESENT ± 2 STANDARD DEVIATIONS.	67
FIGURE 31 COMPARISON OF ORGAN DOSES MEASURED WITH TLDs (BLUE) AND COMPUTED WITH <i>PCXMC</i> SOFTWARE (RED) FOR DR ACQUISITIONS PERFORMED WITH THE LOW-DOSE PROTOCOL OPTIMIZED FOR FOLLOW-UP. ERROR BARS REPRESENT ± 2 STANDARD DEVIATIONS.....	67
FIGURE 33 RELATIVE PERCENTAGE DIFFERENCES BETWEEN DOSE MEASURED WITH TLDs AND THAT COMPUTED WITH MC SIMULATIONS. BLUE, GREEN AND RED COLUMNS REFER TO EOS (SPEED LEVEL 2), CT, AND DR, RESPECTIVELY.....	68
FIGURE 34 COMPARISON OF ORGAN DOSES OF DR ACQUISITIONS PERFORMED WITH THE DIAGNOSIS PROTOCOL (BLUE), AND OF EOS EXAMINATIONS AT SPEED LEVELS 2 (RED), 3 (GREEN), AND 4 (PURPLE).	

DR DOSES WERE COMPUTED WITH MC SIMULATIONS; EOS DOSES WERE INSTEAD DERIVED FROM EXPERIMENTAL MEASUREMENTS WITH TLDs. IN BOTH CASES ERROR BARS REPRESENT TWO STANDARD DEVIATIONS.....	70
FIGURE 35 COMPARISON OF ORGAN DOSES OF DR ACQUISITIONS PERFORMED WITH THE FOLLOW-UP PROTOCOL (BLUE), AND OF EOS EXAMINATIONS AT SPEED LEVELS 2 (RED), 3 (GREEN), AND 4 (PURPLE). FOR EACH TECHNIQUE DOSES WERE DERIVED FROM MEASUREMENTS WITH TLDs. IN BOTH CASES ERROR BARS REPRESENT TWO STANDARD DEVIATIONS.....	71
FIGURE 36 COMPARISON OF EFFECTIVE DOSES. FOR DR EXAMINATION PERFORMED WITH THE DIAGNOSIS PROTOCOL, DOSE ESTIMATED WITH MC SIMULATION IS CONSIDERED. FOR THE OTHER TECHNIQUES, DOSES DERIVED FROM TLD MEASUREMENTS ARE SELECTED. THE LABEL ABOVE EACH COLUMN SHOWS THE REGISTERED VALUE \pm 2 STANDARD DEVIATIONS.....	72

The Tables

TABLE 1 INTERNAL ORGANS PROVIDED WITH HOLES FOR DETECTOR PLACEMENT AND NUMBER OF ALLOWED DOSIMETERS FOR THE 5-YEAR-OLD DOSIMETRY PHANTOM MODEL.....	18
TABLE 2 DAP VALUES (MGY CM ²) OF EOS AP AND LL PROJECTIONS, ACQUIRED AT THREE SPEED LEVELS.....	22
TABLE 3 PARAMETERS OF CONVENTIONAL RADIOGRAPHY ACQUISITIONS. THE SAME kVP AND MAs WERE AUTOMATICALLY SET BY THE SYSTEM FOR EACH CONFIGURATION. DAP VALUES (MGY CM ²) ARE COMPUTED AS THE AVERAGE OF THOSE OBTAINED IN THE ACQUISITIONS OF THE FIVE CONFIGURATIONS OF THE PHANTOM.	23
TABLE 4 ACQUISITION PARAMETERS OF TOPOGRAMS AND WHOLE-BODY SCAN.....	25
TABLE 5 DAP (MGY CM ²) AND kVP OF CONVENTIONAL RADIOGRAPHY AP AND LL PROJECTIONS OBTAINED WITH THE DIAGNOSTIC AND FOLLOW-UP ACQUISITION PROTOCOLS.....	28
TABLE 6 SETUP PARAMETERS USED FOR <i>PCXMC</i> SIMULATIONS OF EOS ACQUISITIONS. PARAMETERS WERE SELECTED TO REPRODUCE EXPERIMENTAL ACQUISITIONS DESCRIBED IN SECTION 2.3.C.....	33
TABLE 7 SETUP PARAMETERS USED FOR <i>PCXMC</i> SIMULATIONS OF DR ACQUISITIONS. <i>UPPER</i> AND <i>LOWER</i> REFER TO ACQUISITIONS OF THE UPPER AND LOWER BODY REGIONS. PARAMETERS WERE SELECTED TO REPRODUCE EXPERIMENTAL ACQUISITIONS DESCRIBED IN SECTION 2.3.C.....	35
TABLE 8 LIST OF THE ORGANS INVESTIGATED WITH DOSIMETRIC IN-PHANTOM MEASUREMENTS; FOR EACH ORGAN, THE NUMBER OF EMPLOYED TLDs IS REPORTED. *FOR SKIN DOSE EVALUATION FOUR CARDS WERE PLACED ON THE PHANTOM SURFACE.....	40

TABLE 9 TISSUE WEIGHTING FACTORS RECOMMENDED BY ICRP 103. FOR A MALE PATIENT, REMAINDER TISSUES INCLUDE ADRENALS, EXTRATHORACIC REGION, GALLBLADDER, HEART, KIDNEYS, LYMPHATIC NODES, MUSCLE, ORAL MUCOSA, PANCREAS, PROSTATE, SMALL INTESTINE, SPLEEN, AND THYMUS.....	43
TABLE 10 MEASURED AVERAGE HUS OF SIMULATED ENCHONDROMAS, PEDIATRIC CARTILAGE AND BONE, AND PHANTOM BONE. THE REPORTED ERROR REPRESENTS ONE STANDARD DEVIATION.	44
TABLE 11 SdNR OF BONE ELEMENTS EVALUATED FROM DR IMAGES OBTAINED WITH THE FOLLOW-UP AND THE DIAGNOSIS ACQUISITION PROTOCOLS.....	52
TABLE 12 EFFECTIVE DOSES (μSv) COMPUTED BY <i>PCXMC</i> FOR EOS ACQUISITIONS AT DIFFERENT SPEED LEVELS, WITH FINITE AND INFINITE FSD. RESULTS OBTAINED WITH BOTH ICRP 60 AND ICRP 103 TISSUE WEIGHTING FACTORS ARE REPORTED. ERRORS REFER TO 2 STANDARD DEVIATIONS.	53
TABLE 13 TUBE PEAK POTENTIALS SELECTED FOR THE CALIBRATION OF DOSIMETERS. FOR EACH VALUE, A BRIEF EXPLANATION IS PROPOSED.....	61
TABLE 14 PARAMETERS OF THE CALIBRATION CURVES. ERRORS REPRESENT ONE STANDARD DEVIATION.....	62
TABLE 15 EFFECTIVE DOSE (μSv) DERIVED FROM MEASUREMENTS WITH TLDs AND PROVIDED BY MC SIMULATIONS FOR EACH IMAGING TECHNIQUE AND ACQUISITION PROTOCOL. ERRORS REPRESENT ± 2 STANDARD DEVIATIONS.	72
TABLE 16 LIFETIME ATTRIBUTABLE RISK (LAR) OF CANCER INCIDENCE (PERCENTAGE VALUE) FOR THE INVESTIGATED IMAGING TECHNIQUES AND ACQUISITION PROTOCOLS. RISKS DERIVED FROM NOMINAL RISK COEFFICIENTS PROVIDED BY BEIR VII, WALL ET AL. (2011), AND ICRP 103 ARE REPORTED.	73

Chapter 5 Bibliography

- [1] ICRP. Radiological protection in paediatric diagnostic and interventional radiology. ICRP Publication 121. vol. 42. 2013.
- [2] ICRP. 1990 Recommendations of the International Commission on Radiological Protection. ICRP Publication 60. vol. 21. 1990.
- [3] European Parliament. Council Directive 2013/59/Euratom of 5 December 2013 laying down basic safety standards for protection against the dangers arising from exposure to ionising radiation, and repealing Directives 89/618/Euratom, 90/641/Euratom, 96/29/Euratom, 97/43/Euratom a. Off J Eur Commun L13 2014:1–73.
- [4] Strauss KJ, Kaste SC. The ALARA (as low as reasonably achievable) concept in pediatric interventional and fluoroscopic imaging: Striving to keep radiation doses as low as possible during fluoroscopy of pediatric patients - A white paper executive summary. *Pediatr Radiol* 2006;36:110–2. <https://doi.org/10.1007/s00247-006-0184-4>.
- [5] Demaio DN, Herrmann T, Noble LB, Orth D, Peterson P, Young J, et al. Best practices in digital radiography. *Radiol Technol* 2019;91:198–201.
- [6] European Commission. European Guidelines on Diagnostic Reference Levels for Paediatric Imaging. vol. 185. 2018. <https://doi.org/10.2833/003998>.
- [7] ICRP. Managing Patient Dose in Digital Radiography. ICRP Publication 93. vol. 34. 2004.
- [8] Damet J, Fournier P, Monnin P, Sans-Merce M, Ceroni D, Zand T, et al. Occupational and patient exposure as well as image quality for full spine examinations with the EOS imaging system. *Med Phys* 2014;41. <https://doi.org/10.1118/1.4873333>.

- [9] Branchini M, del Vecchio A, Gigliotti CR, Loria A, Zerbi A, Calandrino R. Organ doses and lifetime attributable risk evaluations for scoliosis examinations of adolescent patients with the EOS imaging system. *Radiol Medica* 2018;123:305–13. <https://doi.org/10.1007/s11547-017-0828-5>.
- [10] Pedersen PH, Petersen AG, Estgaard SE, Tvedebrink T, Eiskjær SP. EOS micro-dose protocol: First full-spine radiation dose measurements in anthropomorphic phantoms and comparisons with EOS standard-dose and conventional digital radiology. *Spine (Phila Pa 1976)* 2018;43:E1313–21. <https://doi.org/10.1097/BRS.0000000000002696>.
- [11] Deschênes S, Charron G, Beaudoin G, Labelle H, Dubois J, Miron MC, et al. Diagnostic imaging of spinal deformities: Reducing patients radiation dose with a new slot-scanning X-ray imager. *Spine (Phila Pa 1976)* 2010;35:989–94. <https://doi.org/10.1097/BRS.0b013e3181bdcaa4>.
- [12] Somoskeöy S, Tunyogi-Csapó M, Bogyó C, Illés T. Accuracy and reliability of coronal and sagittal spinal curvature data based on patient-specific three-dimensional models created by the EOS 2D/3D imaging system. *Spine J* 2012;12:1052–9. <https://doi.org/10.1016/j.spinee.2012.10.002>.
- [13] Morel B, Moueddeb S, Blondiaux E, Richard S, Bachy M, Vialle R, et al. Dose, image quality and spine modeling assessment of biplanar EOS micro-dose radiographs for the follow-up of in-brace adolescent idiopathic scoliosis patients. *Eur Spine J* 2018;27:1082–8. <https://doi.org/10.1007/s00586-018-5464-9>.
- [14] Lau LCM, Hung ALH, Chau WW, Hu Z, Kumar A, Lam TP, et al.

Sequential spine-hand radiography for assessing skeletal maturity with low radiation EOS imaging system for bracing treatment recommendation in adolescent idiopathic scoliosis: A feasibility and validity study. *J Child Orthop* 2019;13:385–92. <https://doi.org/10.1302/1863-2548.13.190007>.

- [15] Abdi AJ, Mussmann B, Mackenzie A, Klaerke B, Andersen PE. Comparison of radiation exposure to the patient and contrast detail resolutions across low dose 2D/3D slot scanner and two conventional digital radiography X-ray imaging systems. *Radiat Prot Dosimetry* 2019;185:252–65. <https://doi.org/10.1093/rpd/ncz006>.
- [16] Law M, Ma WK, Chan E, Lau D, Mui C, Cheung K, et al. Evaluation of cumulative effective dose and cancer risk from repetitive full spine imaging using EOS system: Impact to adolescent patients of different populations. *Eur J Radiol* 2017;96:1–5. <https://doi.org/10.1016/j.ejrad.2017.09.006>.
- [17] Luo TD, Stans AA, Schueler BA, Larson AN. Cumulative radiation exposure with EOS imaging compared with standard spine radiographs. *Spine Deform* 2015;3:144–50. <https://doi.org/10.1016/j.jspd.2014.09.049>.
- [18] Hamzian N. Equivalent Dose and Risk of Exposure Induced Cancer Death of Different Organs due to Various Image Techniques of EOS Imaging System. *J Biomed Phys Eng* 2021;11:289–96. <https://doi.org/10.31661/jbpe.v0i0.2012-1242>.
- [19] Hui SCN, Pialasse JP, Wong JYH, Lam T ping, Ng BKW, Cheng JCY, et al. Radiation dose of digital radiography (DR) versus micro-dose x-ray (EOS) on patients with adolescent idiopathic scoliosis: 2016 SOSORT-IRSSD “John Sevastic Award” Winner in Imaging Research. *Scoliosis*

Spinal Disord 2016;11:1–8. <https://doi.org/10.1186/s13013-016-0106-7>.

- [20] Kaasalainen T, Palmu K, Lampinen A, Kortnesniemi M. Effect of vertical positioning on organ dose, image noise and contrast in pediatric chest CT - Phantom study. *Pediatr Radiol* 2013;43:673–84. <https://doi.org/10.1007/s00247-012-2611-z>.
- [21] Feng ST, Law MWM, Huang B, Ng S, Li ZP, Meng QF, et al. Radiation dose and cancer risk from pediatric CT examinations on 64-slice CT: A phantom study. *Eur J Radiol* 2010;76:e19–23. <https://doi.org/10.1016/j.ejrad.2010.03.005>.
- [22] Fujii K, Aoyama T, Yamauchi-Kawaura C, Koyama S, Yamauchi M, Ko S, et al. Radiation dose evaluation in 64-slice CT examinations with adult and paediatric anthropomorphic phantoms. *Br J Radiol* 2009;82:1010–8. <https://doi.org/10.1259/bjr/13320880>.
- [23] Nishizawa K, Mori SI, Ohno M, Yanagawa N, Yoshida T, Akahane K, et al. Patient dose estimation for multi-detector-row CT examinations. *Radiat Prot Dosimetry* 2008;128:98–105. <https://doi.org/10.1093/rpd/ncm244>.
- [24] Alrehily F, Hogg P, Twiste M, Johansen S, Tootell A. Scoliosis imaging: An analysis of radiation risk in the CT scan projection radiograph and a comparison with projection radiography and EOS. *Radiography* 2019;25:e68–74. <https://doi.org/10.1016/j.radi.2019.02.005>.
- [25] Fletcher CD, Unni KK, Mertens F. Pathology and genetics of tumours of soft tissue and bone. *Iarc*; 2002.
- [26] Albano D, Loria A, Fanciullo C, Bruno A, Messina C, Del Vecchio A, et al. Diagnostic performance and radiation dose of the eos system to image enchondromatosis: A phantom study. *Appl Sci* 2020;10:1–8.

<https://doi.org/10.3390/app10248941>.

- [27] Number of live births in the EU n.d. <https://www.statista.com/statistics/253401/number-of-live-births-in-the-eu/>.
- [28] Verdegaal SHM, Bovée JVMG, Pansuriya TC, Grimer RJ, Ozger H, Jutte PC, et al. Incidence, Predictive Factors, and Prognosis of Chondrosarcoma in Patients with Ollier Disease and Maffucci Syndrome: An International Multicenter Study of 161 Patients. *Oncologist* 2011;16:1771–9. <https://doi.org/10.1634/theoncologist.2011-0200>.
- [29] Liu J, Hudkins PG, Swee RG, Unni KK. Bone sarcomas associated with ollier's disease. *Cancer* 1987;59:1376–85. [https://doi.org/10.1002/1097-0142\(19870401\)59:7<1376::AID-CNCR2820590725>3.0.CO;2-F](https://doi.org/10.1002/1097-0142(19870401)59:7<1376::AID-CNCR2820590725>3.0.CO;2-F).
- [30] Silve C, Jüppner H. Ollier disease. *Orphanet J Rare Dis* 2006;1:1–6. <https://doi.org/10.1186/1750-1172-1-37>.
- [31] Melhem E, Assi A, El Rachkidi R, Ghanem I. EOS® biplanar X-ray imaging: concept, developments, benefits, and limitations. *J Child Orthop* 2016;10:1–14. <https://doi.org/10.1007/s11832-016-0713-0>.
- [32] Le Bras A, Laporte S, Mitton D, De Guise JA, Skalli W. Three-dimensional (3D) detailed reconstruction of human vertebrae from low-dose digital stereoradiography. *Eur J Orthop Surg Traumatol* 2003;13:57–62. <https://doi.org/10.1007/s00590-003-0074-5>.
- [33] Newton PO, Khandwala Y, Bartley CE, Reighard FG, Bastrom TP, Yaszay B. New EOS Imaging Protocol Allows a Substantial Reduction in Radiation Exposure for Scoliosis Patients. *Spine Deform* 2016;4:138–44. <https://doi.org/10.1016/j.jspd.2015.09.002>.

- [34] Ilharreborde B, Ferrero E, Alison M, Mazda K. EOS microdose protocol for the radiological follow-up of adolescent idiopathic scoliosis. *Eur Spine J* 2016;25:526–31. <https://doi.org/10.1007/s00586-015-3960-8>.
- [35] Pedersen PH, Vergari C, Alzakri A, Vialle R, Skalli W, Skalli WA. A reduced micro-dose protocol for 3D reconstruction of the spine in children with scoliosis: results of a phantom-based and clinically validated study using stereo-radiography. *Eur Radiol* 2019;29:1874–81. <https://doi.org/10.1007/s00330-018-5749-8>.
- [36] ATOM® Dosimetry Phantoms Reference manual n.d.
- [37] Acr–Spr Practice Parameter for the Performance of Computed Tomography (Ct) of the Abdomen and Computed Tomography (Ct) of the Pelvis. *Am Coll Radiol* 2014;1076:1–18.
- [38] Padovani R, Compagnone G, Orlacchio A, Bernardi G, De Ponti E, Cristina Marzola M, et al. Livelli diagnostici di riferimento per la pratica nazionale di radiologia diagnostica e interventistica e di medicina nucleare diagnostica. Aggiornamento del Rapporto ISTISAN 17/33. 2020.
- [39] Bland JM, Altman D. Statistical methods for assessing agreement between two methods of clinical measurement. *Lancet* 1986;327:307–10.
- [40] Mothiram U, Brennan PC, Lewis SJ, Moran B, Robinson J. Digital radiography exposure indices: A review. *J Med Radiat Sci* 2014;61:112–8. <https://doi.org/10.1002/jmrs.49>.
- [41] Tapiovaara M, Lakkisto M, Servomaa A, Siiskonen T. A pc based Monte Carlo program for calculating patient doses in medical x-ray examinations. 1997.

- [42] Eckerman KF, Cristy M, Ryman JC. The ORNL mathematical phantom series. Oak Ridge, TN Oak Ridge Natl Lab 1996.
- [43] ICRP. The 2007 Recommendations of the International Commission on Radiological Protection. ICRP Publication 103. vol. 37. 2007.
- [44] Beir VII. Health risks from exposure to low levels of ionizing radiation. Natl Acad Rep Br 2005.
- [45] Ding A, Gao Y, Liu H, Caracappa PF, Long DJ, Bolch WE, et al. VirtualDose: A software for reporting organ doses from CT for adult and pediatric patients. *Phys Med Biol* 2015;60:5601–25. <https://doi.org/10.1088/0031-9155/60/14/5601>.
- [46] Law M, Ma WK, Lau D, Cheung K, Ip J, Yip L, et al. Cumulative effective dose and cancer risk for pediatric population in repetitive full spine follow-up imaging: How micro dose is the EOS microdose protocol? *Eur J Radiol* 2018;101:87–91. <https://doi.org/10.1016/j.ejrad.2018.02.015>.
- [47] Golikov V, Barkovsky A, Wallström E, Cederblad Å. A comparative study of organ doses assessment for patients undergoing conventional X-ray examinations: phantom experiments vs. calculations. *Radiat Prot Dosimetry* 2018;178:223–34. <https://doi.org/10.1093/rpd/ncx102>.
- [48] Khelassi-Toutaoui N, Berkani Y, Tsapaki V, Toutaoui AEK, Merad A, Frahi-Amroun A, et al. Experimental evaluation of PCXMC and prepare codes used in conventional radiology. *Radiat Prot Dosimetry* 2008;131:374–8. <https://doi.org/10.1093/rpd/ncn183>.
- [49] Lee C, Lee SS, Kim JE, Huh KH, Yi WJ, Heo MS, et al. Comparison of dosimetry methods for panoramic radiography: thermoluminescent dosimeter measurement versus personal computer–based Monte Carlo method calculation. *Oral Surg Oral Med Oral Pathol Oral Radiol*

2016;121:322–9. <https://doi.org/10.1016/J.OOOO.2015.10.030>.

- [50] Wall BF, Haylock R, Jansen JTM, Hillier MC, Hart D. Radiation Risks from Medical X-ray Examinations as a Function of the Age and Sex of the Patient. 2011.
- [51] Gazzetta Ufficiale della Repubblica Italiana. DECRETO LEGISLATIVO 31 luglio 2020, n. 101. 2020.
- [52] Ben Abdennebi A, Aubry S, Ounalli L, Fayache MS, Delabrousse E, Petegnief Y. Comparative dose levels between CT-scanner and slot-scanning device (EOS system) in pregnant women pelvimetry. *Phys Medica* 2017;33:77–86. <https://doi.org/10.1016/j.ejmp.2016.12.008>.
- [53] Hurwitz LM, Yoshizumi T, Reiman RE, Goodman PC, Paulson EK, Frush DP, et al. Radiation dose to the fetus from body MDCT during early gestation. *Am J Roentgenol* 2006;186:871–6. <https://doi.org/10.2214/AJR.04.1915>.
- [54] Clavel AH, Thevenard-Berger P, Verdun FR, Létang JM, Darbon A. Organ radiation exposure with EOS: GATE simulations versus TLD measurements. *Med Imaging 2016 Phys Med Imaging* 2016;9783:978352. <https://doi.org/10.1117/12.2217097>.